LA-UR-18-28644 (Accepted Manuscript)

Simulation of Wingtip Vortex Flows with Reynolds-Averaged Navier–Stokes and Scale-Resolving Simulation Methods

Soares Pereira, Filipe Miguel
Eca, Luis
Vaz, Guilherme

To be published in: AIAA Journal

DOI to publisher's version: 10.2514/1.J057512

Permalink to record: http://permalink.lanl.gov/object/view?what=info:lanl-repo/lareport/LA-UR-18-28644

Simulation of Wingtip Vortex Flows with RANS and SRS Methods

Filipe S. Pereira* and Luís Eça†
Instituto Superior Técnico, Lisbon, 1049-001, Portugal

Guilherme Vaz‡
Maritime Research Institute Netherlands, Wageningen, 6708 PM, The Netherlands

The simulation of wingtip vortex flows is investigated with Reynolds-Averaged Navier-Stokes equations (RANS) and Scale-Resolving Simulation (SRS) models. These range from turbulent viscosity and Reynolds-Stress Model (RSM) RANS closures, to hybrid and bridging SRS methods. The objective of the study is threefold: assess the relevance of replicating the experimental flow conditions; evaluate the numerical requisites of each mathematical model; and determine their modeling accuracy in prediction of a representative wingtip vortex flow. The selected problem is the flow around a NACA0012 wing at ten degrees of angle of attack and Reynolds number of 4.60×10^6. The results confirm the relevance of reproducing the experimental flow conditions, in particular at the inlet boundary where the flow is not uniform. For this reason, the evaluation of modelling errors using the available measurements requires the specification of the experimental inlet conditions. On the other hand, the quantification of the modeling error indicates that solely RANS-RSM can achieve an accurate representation of the flow dynamics. Whereas the well-recognized limitations of turbulent viscosity RANS closures to deal with solid-body rotation lead to the overprediction of turbulence and consequent rapid diffusion of the wingtip vortex, the predictive use of SRS methods may reveal excessively complex and demanding.

*Researcher, Mechanical Engineering, Av. Rovisco Pais 1, Lisbon, Portugal.
†Assistant Professor, Mechanical Engineering, Av. Rovisco Pais 1, Lisbon, Portugal.
‡Senior Researcher, R&D Department, Haagsteeg 2, Wageningen, The Netherlands.

Nomenclature

a_o	=	speed of sound, m/s
c	=	chord, m
C	=	Courant number
C_D	=	pressure drag coefficient
C_F	=	friction drag coefficient
C_L	=	pressure lift coefficient
C_p	=	pressure coefficient
d	=	wall distance, m
E_c	=	comparison error
f_ϵ	=	modeled-to-total ratio of turbulence dissipation
f_k	=	modeled-to-total ratio of turbulence kinetic energy
f_ω	=	modelled-to-total ratio of specific turbulence dissipation rate
g_i	=	spatio-temporal (grid) resolution i
I	=	turbulence intensity
k	=	specific turbulence kinetic energy, m^2/s^2
l_t	=	turbulent length scale, m
l_t^{RANS}	=	RANS or integral turbulent length scale, m
L	=	integral length scale, m
L_∞	=	infinity norm
L_i	=	Cartesian component of the domain length, m
N_c	=	number of cells
P_∞	=	freestream reference pressure, $kg/(m.s^2)$
Q	=	Q-criterion, 1/s
r_i	=	refinement ratio of grid i
r/r_{ref}	=	nondimensional multivariate metric
Re	=	Reynolds number based on the chord c
S_{ij}	=	strain-rate tensor, 1/s
U_e	=	experimental uncertainty
U_n	=	numerical uncertainty
U_v	=	validation uncertainty
$v_i v_j$	=	specific Reynolds-stress tensor, m^2/s^2

V_i = Cartesian velocity component, m/s

V_∞ = freestream reference velocity, m/s

T_∞ = ambient reference temperature, K

x_1^c = streamwise Cartesian coordinate along the wing's chord, m

x_i = Cartesian coordinate, m

x_n^+ = maximum nondimensional wall-normal cell length in wall units

x_s^+ = maximum nondimensional wall-spanwise cell length in wall units

x_t^+ = maximum nondimensional wall-tangential cell length in wall units

α = incoming flow angle, deg

δ = boundary-layer thickness, m

δ_{ij} = Kronecker symbol

Δt = time-step, s

ΔT = sampling time, s

ν = molecular kinematic viscosity, m^2/s

ν_t = turbulent kinematic viscosity, m^2/s

ω = specific turbulence dissipation rate, 1/s

Φ = general quantity

$\overline{\Phi}$ = time-averaged quantity Φ

Φ_e = experimental measurement of quantity Φ

Φ_r = resolved fraction of predicted quantity Φ

Φ_u = unresolved fraction of predicted quantity Φ

ρ = density, kg/m^3

I. Introduction

The relevance of wingtip flows is well recognized in a wide range of practical problems of fluid mechanics. In aeronautical applications [1], for instance, the characteristics of the resultant wingtip vortex dictate the time interval between aircraft landings or take-offs; the flying distance separating successive aircrafts; or the magnitude of the vibrations experienced by helicopter blades. In marine engineering, on the other hand, these coherent structures can cause cavitation inception [2], erosion on downstream structures, and harmful vibrations. Along with the former problems, noise and losses in energy efficiency also pose great concern for both economic and environmental reasons.

The importance of wingtip vortices to practical applications have therefore motivated the conduction of innumerous investigations intended to further understand the dynamics of such phenomena. The studies of Grow [3], Mehta and Cantwell [4], Chigier and Corsiglia [5], Stinebring et al. [6], Devenport et al. [7], and Chow et al. [8] are examples of important experimental contributions. In regard to numerical simulations, Srinivasan et al. [9], de Jong et al. [10], and Dacles-Mariani et al. [11, 12] are cases of pioneering studies in this area. However, measuring and examining wingtip vortices is a challenging assignment. For configurations of practical interest, the dynamics of these flows might entail a laminar boundary-layer; turbulence onset; turbulence; three-dimensional local flow separation; vortices formation, interaction, merging, and roll-up; meandering; free shear-layers; and wake. All these phenomena are strongly dependent on boundary conditions.

The former set of features pose various difficulties to the numerical simulation of this class of flows. From a numerical perspective, the accurate representation of wingtip vortices and their large gradients require high-quality discretizations - schemes accuracy, spatio-temporal resolution and grid topology. From a modeling standpoint, on the other hand, turbulence modeling is usually the major contributor to the modeling error. This stems from the inability of most turbulence closures based on the Boussinesq hypothesis to predict the near solid-body rotation with low intensity turbulence of the wingtip vortex inner core. For this reason, the combination of such closures with Reynolds-Averaged Navier-Stokes equations (RANS) tends to overpredict the Reynolds-stress tensor and assumes that its shear components are aligned with the time-averaged strain-rate tensor [13, 14]. The alternative is using Reynolds-Stress Model (RSM or second-moment) based closures [15–17] or Scale-Resolving Simulation (SRS) methods [18–20] owing to their ability to predict such practical configurations. However, whereas the numerical stiffness of RSM closures [21–24] might pose difficulties to reduce the iterative error to adequate levels, the demanding numerical requisites of SRS methods [25] as well as their dependency on inlet boundary conditions [25, 26] and turbulence onset hamper their predictive use.

The consequences of the aforementioned difficulties are illustrated in figure 1. This figure presents a review of numerical results available in literature for the pressure coefficient at a location of the wingtip vortex measured by Chow et al. [8]. In such study, Chow et al. [8] conducted a set of experimental measurements to the flow around a NACA0012 wing at ten degrees of angle of attack and Reynolds number of $Re = 4.6 \times 10^6$ in order to investigate the dynamics of the wingtip vortex and provide validation data. The results are depicted in terms of the mathematical model and number

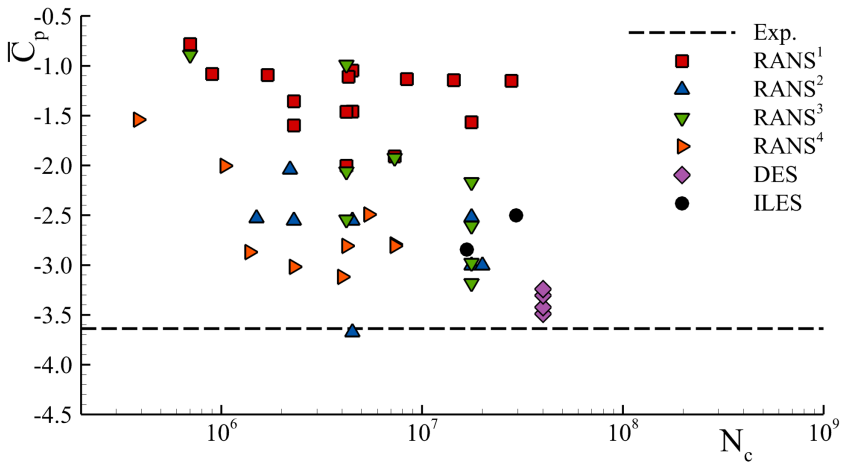

Fig. 1 Literature review of available numerical results for the time-averaged pressure coefficient $\overline{C}_p$ at the wingtip vortex center (x/c = 1.416; 0.056; 0.660) resultant from the flow around a NACA0012 wing at ten degrees of angle of attack and $Re = 4.60 \times 10^6$. Numerical results collected from [11, 12, 15, 16, 18–20, 27–30] and presented as a function of mathematical model and number of grid cells N_c. The superscripts denote distinct RANS closures: 1 - linear turbulent viscosity models; 2 - turbulent viscosity models employing rotation/curvature corrections; 3 - non-linear turbulent viscosity models; 4 - RSM. Experimental data taken from Chow et al. [8].

of grid elements (measure of the spatial resolution). Similar to the literature survey shown in Pereira et al. [31] for a circular cylinder at $Re = 3,900$, the data exhibit a wide range of values for each mathematical model which points out the relevance of the numerical and input error. Yet, the most significant result in figure 1 is the clear improvement of the predictions towards the experimental measurement with the modeling strategy. Whereas traditional turbulent viscosity RANS closures attain a poor agreement with the experiments, RANS-RSM closures and SRS methods are able to significantly reduce the comparison error. This further confirms the relevance of turbulence modeling to the prediction of such class of flows.

The objective of this study is therefore to investigate the requisites and modeling accuracy of various RANS and SRS methods of practical interest to predict a wingtip vortex flow. Towards this end, the representative wingtip vortex flow of Chow et al. [8] is simulated and the resulting discretization and modeling errors quantified. The relevance of replicating the experimental flow conditions is also investigated. This includes the freestream flow conditions, the modeling of the experimental facility walls, and the importance of turbulence onset to SRS computations predicting flow problems where such phenomenon is forced. A total of eight RANS closures and three SRS methods are evaluated. These range from turbulent viscosity and RSM RANS closures, to hybrid and bridging SRS methods.

The remainder of this manuscript is structured as follows. The details of the flow problem and numerical simulations are described in Section II. Thereafter, the results are presented and discussed in Section III. The article concludes in Section IV with the summary of the major findings.

II. Flow Problem and Simulations Details

A. Flow Problem

The selected test case is the wingtip vortex flow measured by Chow et al. [8] with the objective of investigating the dynamics of wingtip vortices and provide reference data for numerical simulations. The experiments have been conducted in a wind tunnel with a cross-section of $1.00c$ (width) by $0.66c$ (height), and a length of $2.5c$. The freestream velocity V_∞ was selected to attain a Reynolds number based on the wing's chord c of 4.60×10^6, and the resultant Mach number was approximately 0.15*. The tested wing has a rectangular planform with a NACA0012 section, an aspect-ratio of 0.75, and a rounded wingtip. The geometric angle of attack is ten degrees and the leading edge is located $0.15c$ downstream the wind tunnel inlet. Despite the inherent blockage effects and non-uniform inlet flow, the model's large dimensions and proximity to the inlet boundary reduce the viscous effects from the boundary-layers of the test-section walls by diminishing the relative boundary-layer thickness δ/c. Furthermore, the model possesses tripping elements at approximately $0.04c$ from the leading edge to force turbulence transition. The consequence of this option is the upstream movement of transition, from the wing's half chord to the leading edge region - figure 2. This should pose great challenges to SRS formulations resolving turbulence in the boundary-layer region due to difficulties replicating forced transition. RANS closures, on the other hand, are expected to take advantage of their well recognized early turbulence transition issues (see Wilcox [32]) to reduce the effects of this option. The quantities measured by Chow et al. [8] used in this study are the time-averaged pressure coefficient $\overline{C}_p$, velocity $\overline{V}_i$, and the Reynolds-stress shear component $\overline{v_1 v_2}$. These quantities have been measured through pressure taps ($\overline{C}_p$ on the wing), seven-hole pressure probes ($\overline{C}_p$ at the wingtip vortex center) and triple hot-wire anemometer ($\overline{V}_i$ and $\overline{v_1 v_2}$) techniques. The reported experimental uncertainties do not exceed 15.0%. It is important to mention that the location of the wingtip vortex center at each streamwise plane has been determined as the point of of lowest crossflow velocity. The details and uncertainties involved in these measurements are summarized in table 1.

B. Simulations Details

The computations are performed with the community based open-usage solver ReFRESCO [33]. The governing equations of the selected RANS and SRS models are written in their strong conservation form and discretized using a finite-volume approach with cell-centered collocated variables. A total of eight distinct RANS closures are evaluated: the one-equation model of Spalart and Allmaras [34] with (SA-C) and without (SA) the rotation correction used by Dacles-Mariani et al. [11]; the two-equation $k-\omega$ closure of Wilcox [35] (W98), the Shear-Stress Transport (SST) of Menter et al. [36], the Turbulent/Non-Turbulent (TNT) of Kok [37], and the Explicit Algebraic Reynolds-Stress Model (EARSM) of Dol et al. [38]; the $k-\sqrt{k}L$ (KSKL) of Menter et al. [39]; and finally the seven-equation RSM closure of Eisfeld and Brodersen [40]. In regard to SRS models, Delayed Detached-Eddy Simulation (DDES) of Gritskevich et al.

*Assuming a speed of sound equal to $a_o = 343m/s$, and an ambient temperature of $T_\infty = 293.15K$.

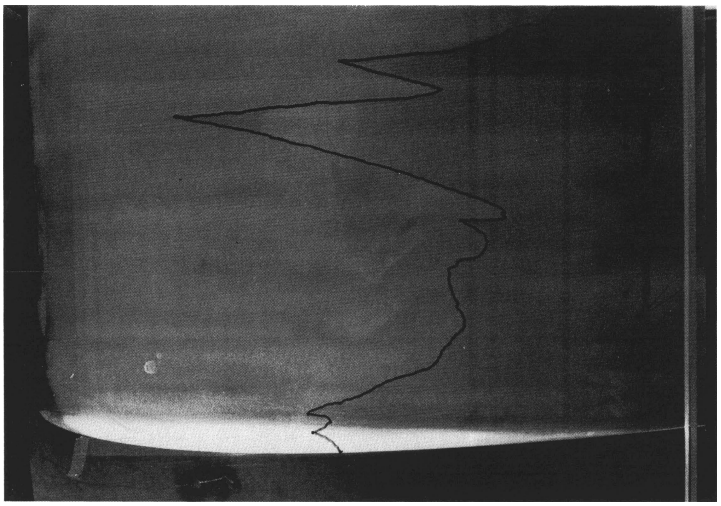

Fig. 2 Location of natural turbulent transition for the NACA0012 wing flow of Chow et al. [8]. Picture taken from Chow et al. [8]. Laminar/turbulent interface delimited by the black line.

Table 1 Experimental measurements details: fluid, Reynolds number Re, inflow turbulence intensity I, facility vertical and spanwise lengths, L_2/c and L_3/c, experimental method, dimensionless sampling time used to converge the flow statistics $\Delta T V_\infty/c$, measured quantity Φ_e, and respective experimental uncertainty $U_e(\Phi_e)$. PT stands for Pressure Tap, PP for seven-hole Pressure Probe, and HWA for triple Hot-Wire Anemometer.

Source	Fluid	Re	$I(\%)$	L_2/c	L_3/c	Method	$\Delta T V_\infty/c$	Φ_e	$U_e(\Phi_e)$
Chow et al. [8]	Air	4.60×10^6	< 0.15	0.66	1.00	PT	170	$\overline{C}_p$	–
						PP	170	$\overline{C}_p$	1.1%
						HWA	850	$\overline{V}_i$	2.0%
								$\overline{v_1 v_2}$	15.0%

[41], Delayed eXtra Large-Eddy Simulation (DXLES) of Kok [42], and Partially-Averaged Navier-Stokes equations (PANS) [43] of Pereira et al. [44] are the analyzed formulations. The selected DDES and PANS formulations model the unresolved turbulent stresses through a modified version of the RANS-SST [36] closure, whereas DXLES uses the TNT [37] closure in RANS mode and a subgrid k-equation closure to represent the unresolved turbulent stresses. A pressure-correction equation based on the SIMPLE algorithm is used to ensure mass conservation. Both spatial and temporal discretization schemes are second-order accurate. The exceptions are the governing equations of the closure models which are discretizated with a first-order accurate upwind scheme. At each implicit time-step, the non-linear system for velocity and pressure is linearised with Picard's method, and a segregated approach is adopted here for the solution of all transport equations. The simulations are run in parallel using MPI and subdomain decomposition.

The numerical simulations are conducted in a hexahedral (rectangular parallelepiped) computational domain defined in a Cartesian coordinate system (x_1, x_2, x_3) - figure 3. The reference frame is centred at the quarter chord point of the wing's root with the x_1 axis aligned with the streamwise flow, the x_2 axis set in the vertical direction, and the x_3 axis

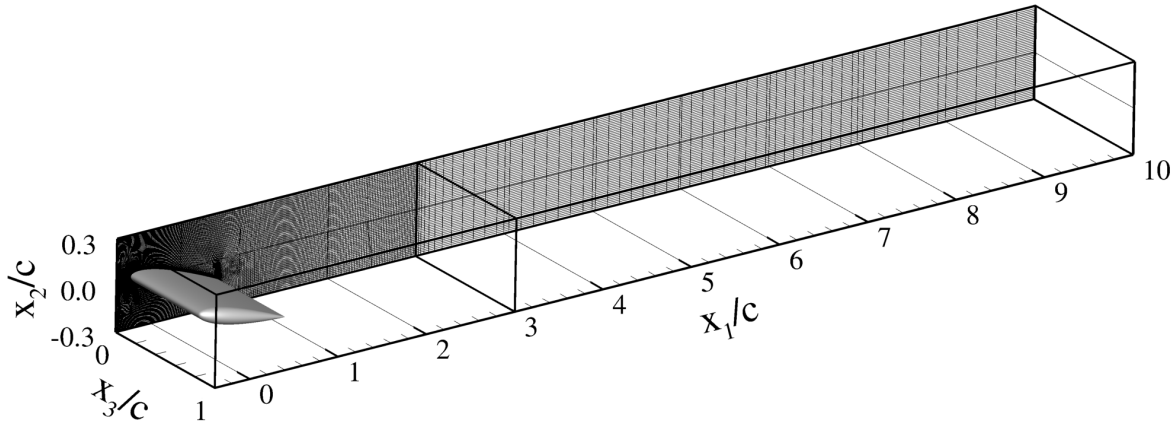

(a) Computational domain (set A).

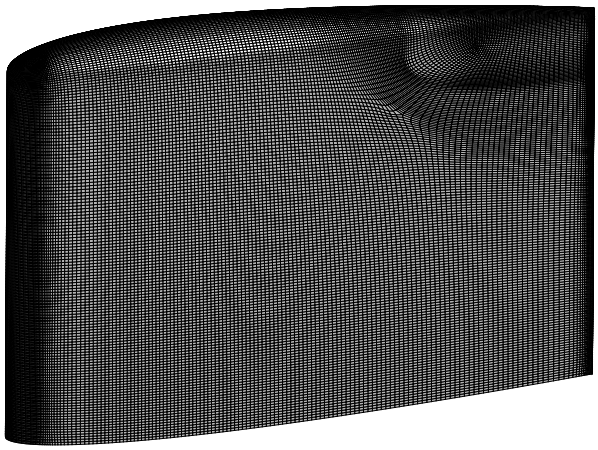

(b) Wing's surface spatial resolution.

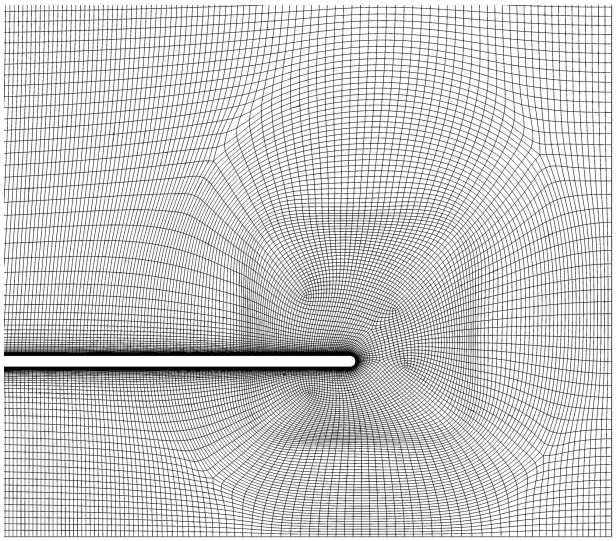

(c) Spatial resolution at $x_1/c = 0.70$.

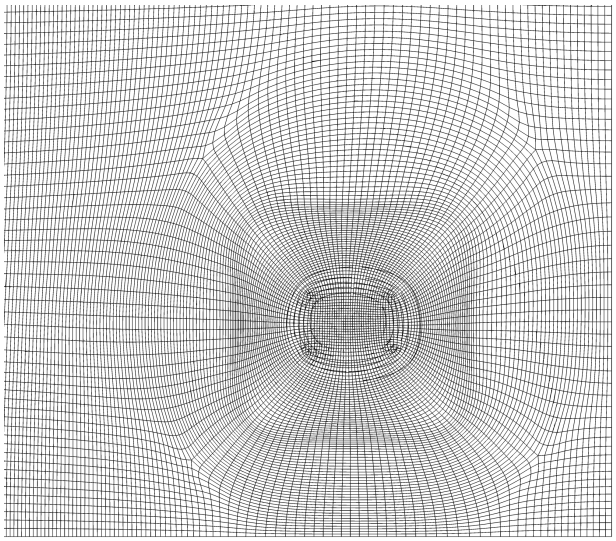

(d) Spatial resolution at $x_1/c = 1.00$.

Fig. 3 Computational domain (set A) and spatial grid resolution g_7.

oriented with the wing's span. The angle of attack is set by rotating the wing ten degrees over the x_3 axis (clock-wise). The cross-section of the computational domain mimics the dimensions of the experimental facility of Chow et al. [8]. Therefore, the vertical and spanwise boundaries are placed at $x_2/c = \pm 0.33$, $x_3/c = 0.0$ and 1.0. The inlet and outlet boundaries are located at $x_1/c = -0.396$ and 10.0, respectively. A second computational domain with an extended inlet boundary is also used to evaluate the influence of the flow conditions applied at this boundary. In that case, the inlet plane is located at $x_1/c = -5.0$.

Two alternatives are tested for the specification of the velocity field at the inlet boundary: *i)* imposing $V_1 = V_\infty$ and setting the remainder velocity components equal to zero; or *ii)* using the available experimental measurements at this location to define V_i. The latter option, however, requires the extrapolation and interpolation of the data of Chow et al. [8]. The resultant V_1 field prescribed at the inlet plane is shown later in figure 5a. Note that the boundary-layers of the test-section walls have been neglected since their features are not available. The pressure, on the other hand, is extrapolated in both cases from the interior of the domain, while the modeled turbulence quantities result from setting the turbulence intensity to $I = 0.15\%$ to replicate the experiments of Chow et al. [8], and a ratio between turbulent and molecular kinematic viscosities of $\nu_t/\nu = 0.78$ to attain $\omega c/V_\infty \approx 20$[†]. In the case of the RSM closure, the components of the Reynolds-stress tensor are estimated from $v_i v_j = 2/3 k \delta_{ij}$, with δ_{ij} being the Kronecker symbol. At the outflow boundary, $x_1/c = 10.0$, the pressure is imposed, and the streamwise derivatives of all the remainder dependent variables are set equal to zero. No-slip and impermeability conditions are specified at the wing's surface. Furthermore, the normal pressure derivative and turbulence dependent quantities are set equal to zero. The exception is the modeled specific dissipation which is defined at the center of the nearest-wall cell as $\omega = 80\nu/d^2$ [35]. At the lateral walls of the domain, the x_2/c and x_3/c planes, the dependent variables are defined by either *i)* setting the normal velocity, the shear components of the Reynolds-stress tensor possessing the same index of the wall plane ($\tau_{ij} = 0$ for an x_i plane,), and the normal derivatives of the remainder dependent variables equal to zero - free-slip condition; or *ii)* using the V_i and P conditions prescribed at the wing's surface (no-slip and impermeability conditions), while the turbulence quantities and shear-stress at the wall are calculated from the wall-function proposed by Menter and Esch [46]. It is important to mention that the parameters modeled-to-total ratio of turbulence kinetic energy f_k and specific dissipation rate f_ω are also used to define the boundary conditions in PANS simulations. In this study, we use $f_k = 0.50$ and assume that dissipation occurs entirely in the unresolved scales so that $f_\omega = 1/f_k$. The influence of the boundary conditions specified at the inlet and lateral walls is discussed in Section III.A.

The main calculations are executed in a group of ten multiblock structured grids here denoted as set A. Their spatial resolution covers a refinement level of 3.90, and range from 942, 120 to 55, 951, 239 hexahedral cells. Note, however, that the two finest grids are only used in RSM calculations due to the larger grid requisites of this closure. Two additional groups of four grids have also been used to investigate the influence of the inlet and lateral walls conditions - sets B

[†]This value possesses the same order of magnitude of that recommended by Menter [45]

Table 2 Grid set A properties, g_i: refinement ratio r_i, maximum dimensionless cell length (wall-units) in the tangential x_t^+, normal x_n^+, and spanwise x_s^+ directions, maximum Courant number C, total number of cells N_c, dimensionless time-step $\Delta t V_\infty/c$, and minimum sampling time to converge the analyzed flow statistics $\Delta T V_\infty/c$. x_i^+ estimated from SST solutions, while C from DDES.

g_i	r_i	x_t^+	x_n^+	x_s^+	C	N_c	$\Delta t V_\infty/c$	$\Delta T V_\infty/c$
g_1	1.00	815.6	0.5	802.7	–	55, 951, 239	–	–
g_2	1.09	885.3	0.6	860.6	–	43, 130, 692	–	–
g_3	1.18	971.0	0.6	931.1	–	32, 609, 052	–	–
g_4	1.33	1079.0	0.7	1051.7	–	23, 536, 656	–	–
g_5	1.50	1208.7	0.8	1265.4	4.8	16, 542, 464	5×10^{-4}	50.0
g_6	1.71	1375.0	0.9	1372.8	–	11, 092, 424	–	–
g_7	2.00	1597.4	1.1	1633.5	–	6, 993, 936	–	–
g_8	2.37	1878.1	1.1	1957.7	–	4, 222, 000	–	–
g_9	2.95	2334.0	1.4	2397.0	–	2, 188, 480	–	–
g_{10}	3.90	2899.2	2.2	3288.9	–	942, 120	–	–

and C. The three grid sets have similar topologies and spatial resolutions at the wing's surface and wake regions. The differences lie on the location of the inlet boundary and on the spatial resolution close to the lateral walls: the length of the computational domain of set B is extended to $15c$, $-5 \leq x_1/c \leq 10$; while set C possesses sufficient grid resolution to apply no-slip conditions at the lateral walls of the domain. The properties of all grid sets are summarized in tables 2 and 3.

All RANS simulations assume steady flow since initial testing demonstrated that steady and time-dependent RANS computations lead to similar results for this statistically steady flow problem. On the other hand, the SRS calculations are evidently time-dependent and carried out on a single spatial grid resolution - g_5. The dimensionless time-step is set equal to 5×10^{-4}, leading to a maximum instantaneous Courant number of 4.8 at the trailing edge of the wing. All time-dependent computations started from a partially converged DXLES solution. Then, whereas DDES computations run for 100 time-units and the sampling time is 50 time-units, DXLES and PANS simulations are conducted only for 10 time-units. These sampling times and the single spatio-temporal resolution are sufficient to accomplish the objectives of this investigation. This point is demonstrated later in Section III.C. Finally, in order to minimize the round-off and iterative error, the simulations are conducted on double precision with an iterative convergence criterion that requires a maximum normalized residual of 10^{-5} for all dependent variables and time instants. In time-dependent simulations, this leads to an averaged number of iterations per time instant close to 56 for PANS ($f_k = 0.50$). The selected iterative criterion is tightened to 10^{-7} in RSM computations. It is important to mention that such criterion was not achieved

Table 3 Grid sets B and C properties, g_i: refinement ratio r_i, maximum dimensionless normal cell length (wall-units) x_n^+, and total number of cells N_c. x_n^+ estimated from SST solutions, and measured on the wing/lateral walls surface.

g_i	Set B			Set C		
	r_i	x_n^+	N_c	r_i	x_n^+	N_c
g_7	1.00	1.2/–	6,349,968	1.00	1.2/22.1	11,475,976
g_8	1.18	1.2/–	3,863,300	1.17	1.2/24.2	7,161,403
g_9	1.47	1.5/–	2,015,552	1.44	1.6/29.9	3,809,440
g_{10}	1.93	2.1/–	876,708	1.90	2.4/38.8	1,671,545

in three grids (g_1, g_2, and g_4) due to the longer wingtip vortex predicted by this closure which moved the maximum residuals to the outlet boundary. Nonetheless, the influence of this aspect on the results is very small since the maximum residuals in the interior of the domain did not exceed $O(10^{-4})$.

III. Results

This section discusses the outcome of the present investigation intended to *i)* evaluate the importance of replicating the experimental flow conditions; *ii)* assess the grid requisites of the selected RANS and SRS methods; and *iii)* quantify the modeling accuracy of each formulation in prediction of the wingtip vortex flow of Chow et al. [8]. To accomplish these objectives, the discretization/numerical uncertainty $U_n(\Phi)$ is estimated with the procedure proposed by Eça and Hoekstra [47] based on grid refinement exercises, while the modeling error is quantified through the comparison error $E_c(\Phi)$ defined as the difference between the prediction Φ and experiment Φ_e. The experimental measurements of Chow et al. [8] are used as reference data. Furthermore, in cases of multiple set points, the multivariate metric r/r_{ref} of Hills [48] is employed to quantify the modeling error. This parameter is defined here as [48, 49]

$$\frac{r}{r_{\text{ref}}} = \sqrt{\frac{\sum_i^N E_c(\Phi_i)^2 U_v(\Phi_i)^{-2}}{N + \sqrt{2N}}}, \tag{1}$$

where N is the number of evaluated points, i is an index denoting a given point, and $U_v(\Phi)$ is the validation uncertainty defined as $U_v(\Phi) = \sqrt{U_e(\Phi_e)^2 + U_n(\Phi)^2}$. It is assumed that the input, iterative and round-off errors are negligible, and that the comparison error at the different points is uncorrelated. The interpretation of this parameter is the following: values of r/r_{ref} exceeding one indicate that the modeling error is globally larger than the validation uncertainty; while the opposite shows that the modeling error is in general within the validation uncertainty.

The section starts by assessing the influence of the flow conditions specified at the inlet and test-section walls - Section III.A. Afterwards, Section III.B compares the RANS predictions against the experiments of Chow et al.[8].

Numerical and modeling errors are estimated. Section III.C concludes the discussion with the SRS results. All the analyzed flow quantities are normalized by V_∞, c, or ρ.

A. Boundary Conditions Effects

1. Inlet Flow Conditions

The wing used in the experiments of Chow et al. [8] is located in the vicinity of the inlet plane to reduce the effects of the test-section's boundary-layers. This strategy, however, has the disadvantage of generating a non-uniform flow at the inlet of the experimental facility, $x_1/c = -0.396$. For this reason, the numerical studies of figure 1 have set the inflow conditions in three distinct forms: *i)* by simply defining uniform inflow conditions that lead to a Reynolds number of 4.60×10^6. Albrecht et al. [28] also suggested that $Re = 4.35 \times 10^6$ would better replicate the experimental conditions of Chow et al.[8]; *ii)* adjusting the location of the inlet plane and Reynolds number in order to obtain a fair agreement between the numerical and experimental velocity field at $x_1/c = -0.396$; and *iii)* imposing the experimental inlet conditions. Although the latter strategy may lead to numerical difficulties, it seems a necessary step to reduce input errors between the numerical setup and the experiments of Chow et al. [8]. The majority of the reported studies used the first option, while only Dacles-Mariani et al. [11, 12] relied on the third strategy.

The relevance of this aspect is investigated here through the execution of RANS simulations using the following settings: case A - impose the experimental velocity field at the inlet of grid set A; case A_1 - define uniform flow conditions at the inlet of grid set A; and case B_1 - apply uniform inlet flow conditions, and use the extended domain of grid set B. The Reynolds number based on the nominal incoming velocity is 4.60×10^6 in all cases. The simulations are performed with the SST and EARSM closures, and the numerical uncertainty is estimated using the four coarsest grids of each set (g_7 to g_{10}). The results for the friction ($\overline{C}_F$) and pressure ($\overline{C}_D$ and $\overline{C}_L$) coefficients are shown in table 4, whereas figure 4 depicts the local pressure coefficient along the wing's chord at two cross-sections. It is important to mention that Chow et al. [8] did not report any details about the reference freestream pressure P_∞. Hence, and considering the irregular pressure field at the inlet plane, the P_∞ used in this work is the value that optimizes the agreement of the predictions of the surface pressure with the experiments at the stagnation region ($\overline{C}_p = 1.0$) for $x_3/c \geq 0.500$[‡]. This is obtained estimating P_∞ from the experimental pressure coefficient distribution at the wing span of $x_3/c = 0.583$. This wing span is used to determine P_∞ for all closures employed in this work. This procedure, however, was not applied in cases A_1 and C_1 due to the combination of an uniform velocity field with a highly irregular pressure field at the inlet. In these cases, P_∞ is simply defined in a manner that guarantees $\overline{C}_p = 1.0$ at the stagnation region. Nonetheless, note that the value of the reference freestream pressure produces only a vertical shift of the pressure coefficient lines.

Referring to table 4, the predictions of the time-averaged friction drag $\overline{C}_F$, pressure drag $\overline{C}_D$ and lift $\overline{C}_L$ coefficients

[‡]For $x_3/c < 0.500$, the effects of the wind tunnel boundary-layers are meaningful to the pressure distribution on the wing's surface. These are neglected in cases A, A_1, and B_1.

Table 4 Time-averaged pressure drag $\overline{C}_D$, friction drag $\overline{C}_F$, and pressure lift $\overline{C}_L$ coefficients and respective numerical uncertainties $U_n(\Phi)$ as a function of the closure and numerical conditions: case A - grid set A and experimental inlet velocity field; case A_1 - grid set A and uniform inlet velocity field; case B_1 - grid set B and uniform inlet velocity field; and case C_1 - grid set C and uniform inlet velocity field. Uncertainties shown as percentage of predicted value. Results in grid g_7.

Closure	Case	$\overline{C}_D \times 10$	$U_n(\overline{C}_D)$	$\overline{C}_F \times 10^2$	$U_n(\overline{C}_F)$	$\overline{C}_L$	$U_n(\overline{C}_L)$
SST	A	0.55	1.1	0.73	3.6	0.57	0.8
	A_1	0.73	2.3	0.96	3.5	0.64	0.6
	B_1	0.53	1.9	0.77	3.2	0.63	1.3
	C_1	0.77	2.0	0.96	4.0	0.64	1.5
EARSM	A	0.55	1.8	0.69	2.4	0.57	2.4
	A_1	0.73	1.3	0.90	2.1	0.64	1.2
	B_1	0.52	5.5	0.73	2.0	0.63	2.4
	C_1	0.77	0.9	0.91	2.4	0.65	0.9
Exp.[§]	-	–	–	–	–	0.51	–

clearly demonstrate the influence of the location and conditions set at the inlet boundary. Independently of the RANS closure, cases A_1 and B_1 lead to an increase in the lift coefficient up to 12%, and a comparison error larger than 24% of the estimated[§] experimental value. The drag coefficients, on the other hand, exhibit a different behavior: whereas cases A and B_1 predict similar values of $\overline{C}_F$ and $\overline{C}_D$, case A_1 causes a significant growth in these two quantities. Note that none of these differences are a consequence of the numerical uncertainty since its magnitude does not exceed 5.5%.

The importance of the inlet boundary is further illustrated by the distribution of the pressure coefficient along the wing's chord at $x_3/c = 0.667$ - figure 4. Whereas simulations using the experimental inlet conditions (set A) are in a good agreement (magnitude and shape) with the experiments, the remainder cases lead to the increase of the area between the pressure and suction side curves. Moreover, cases A_1 and B_1 exhibit significantly higher pressure peaks. In all cases, the mismatches observed at the wingtip vortex region ($x_1^c \geq 0.6$) between simulations and experiments result from modeling errors (see Section III.B.2).

The previous results show the close relation between the inlet conditions and the flow dynamics. To understand the reasoning behind the former differences, figure 5 plots the time-averaged streamwise velocity field $\overline{V}_1$ and the incoming flow angle, $\overline{\alpha} = \arctan(\overline{V}_2/\overline{V}_1)$, at the experimental inlet plane $x_1/c = -0.396$ for cases A and B_1. The data indicate that the discrepancies observed in table 4 and figure 4 arise from differences in the velocity field at the inlet. It is clear that the experiments and the simulations of case A are both conducted with a non-uniform inlet velocity field and incoming flow angle. Furthermore, the figure also indicates that the incoming flow angle does not exceed seven degrees

[§]Chow et al. [8] computed this value from the integration of the pressure coefficient on the wing surface at seven planes along the span.

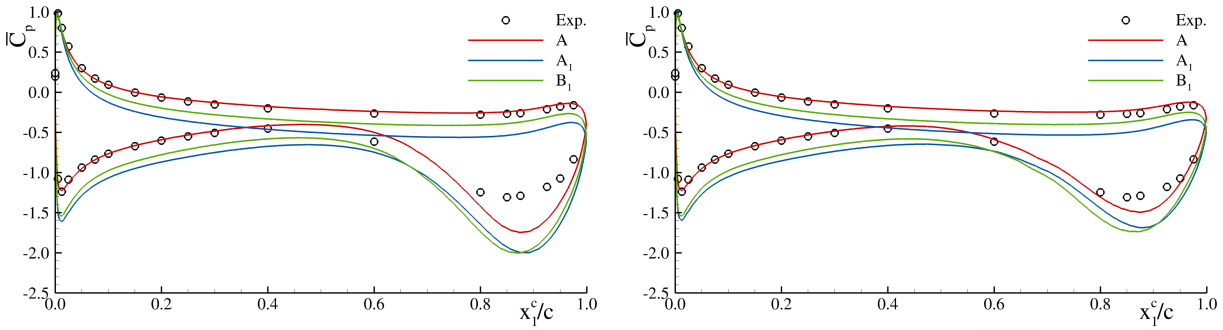

(a) x_3/c = 0.667 - SST. (b) x_3/c = 0.667 - EARSM.

Fig. 4 Time-averaged pressure coefficient along the wing's chord $\overline{C}_p(x_1^c)$ as a function of the closure and numerical conditions: case A - grid set A and experimental inlet velocity field; case A_1 - grid set A and uniform inlet velocity field; and case B_1 - grid set B and uniform inlet velocity field. Results in grid g_7 and at cross-section x_3/c = 0.667.

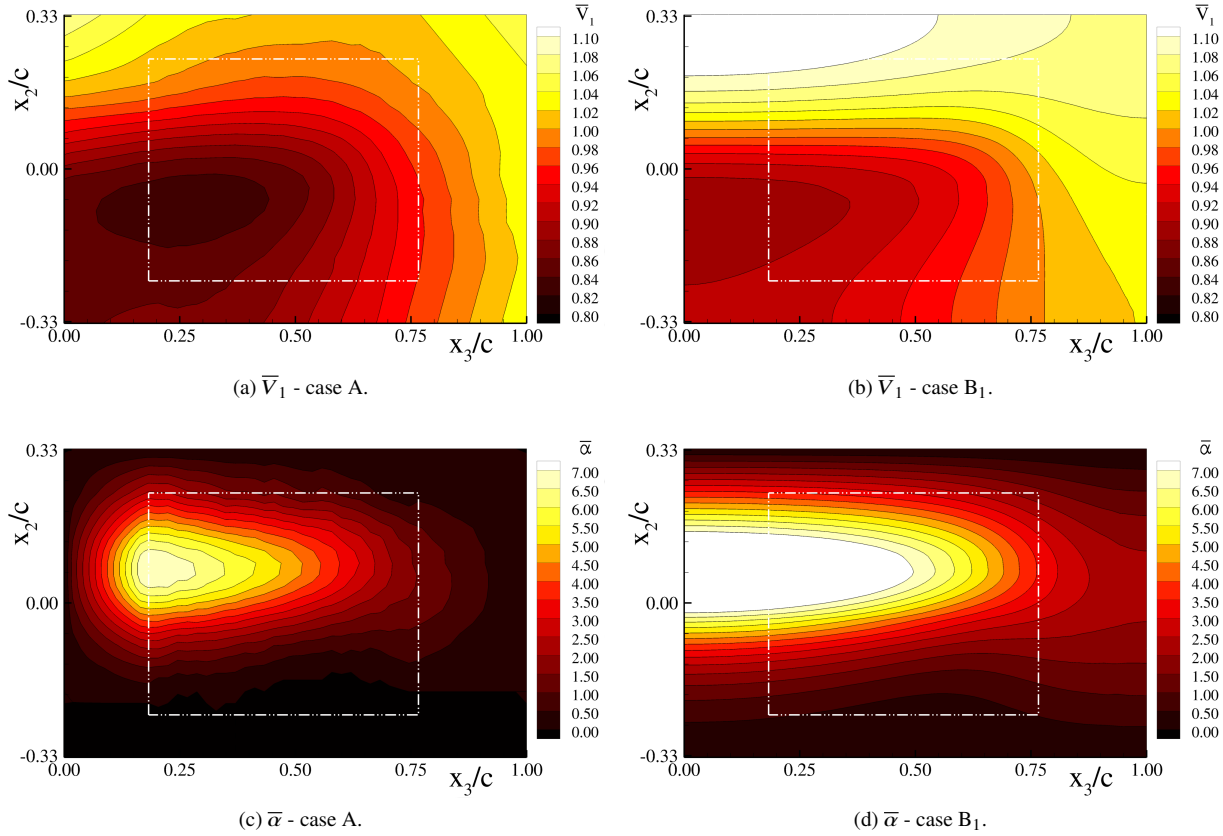

(a) $\overline{V}_1$ - case A. (b) $\overline{V}_1$ - case B_1.

(c) $\overline{\alpha}$ - case A. (d) $\overline{\alpha}$ - case B_1.

Fig. 5 Time-averaged streamwise velocity $\overline{V}_1$ and resultant incoming flow angle $\overline{\alpha}$ (in degrees) with x_1 direction at $x_1/c = -0.396$ for cases A and B_1. Results of case B_1 obtained with SST in grid g_7. White line delimits area where experimental measurements of Chow et al. [8] are available.

for case A, while for case B_1 this quantity grows to approximately nine degrees. Hence, the larger incoming flow angle of cases A_1 and B_1 increases the lift coefficients and leads to distinct distributions of the pressure coefficient along the

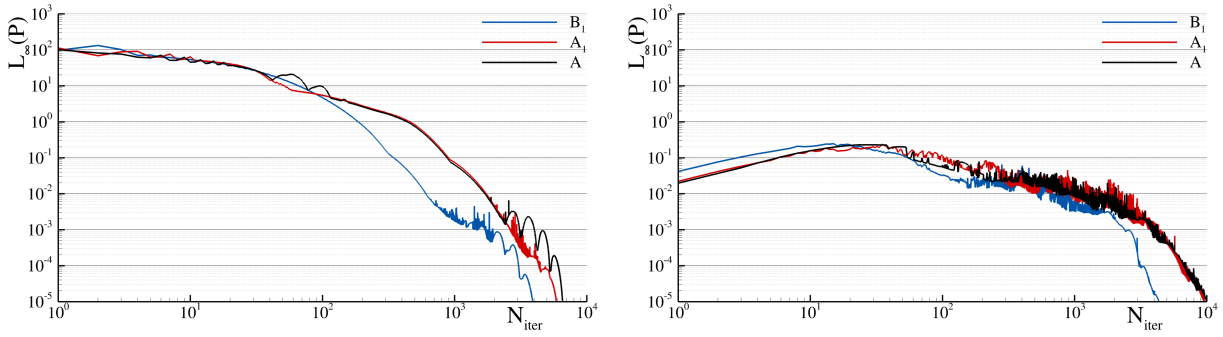

(a) SST. (b) EARSM.

Fig. 6 History of the infinity norm of the pressure residual $L_\infty(P)$. Results for SST and EARSM closures in grid g_7.

wing's surface. The observed differences between drag coefficients in these two cases are a result of imposing uniform conditions at $x_1/c = -0.396$ in case A_1.

Despite the uncertainty related with the wind tunnel boundary-layers, it is shown that setting the experimental conditions is the best manner to predict the present flow problem. Alternative techniques such as adjusting the location of the inlet plane and Reynolds number may minimize the problem but hardly correct all mismatches in the inlet velocity field and incoming flow angle. Regarding the numerical robustness of case A, all simulations converged to the intended iterative convergence criterion ($c_{it} = 10^{-8}$ was also successfully tested). Nonetheless, the necessary number of iterations increased by a factor of approximately two from case B_1 to A. The iterative convergence history is illustrated in figure 6 for the three cases[¶].

2. Test-Section Walls

The form how the lateral walls of the test-section are represented influences the flow blockage and determines the dynamics of the horse-shoe vortex. Considering the objective of the work, the importance of this aspect to the dynamics of the wingtip vortex is here investigated through the execution of RANS simulations using the following two groups of settings: case A_1 - free-slip conditions at the test-section's walls of grid set A; and case C_1 - no-slip conditions at the lateral walls of grid set C. The inlet conditions are set uniform in both cases. All cases are carried out in the four coarsest grids of each set using the SST and EARSM closures.

The results of cases A_1 and C_1 for the friction and pressure coefficients are presented in table 4. Whereas the friction drag and lift coefficients are similar, the pressure drag coefficient exhibits an increase of 5.5% from case A_1 to C_1. This stems from the larger flow blockage. Figure 7, on the other hand, depicts the local pressure coefficient along the wing's chord and wingtip vortex center. The data show that the differences between the two cases are relatively small. For this

[¶]Note that the residuals of EARSM simulations are initially smaller than those obtained with the SST due to the use of the correspondent (A, A_1, and B) converged SST fields as initial solution. SST computations, on the other hand, start from uniform flow fields.

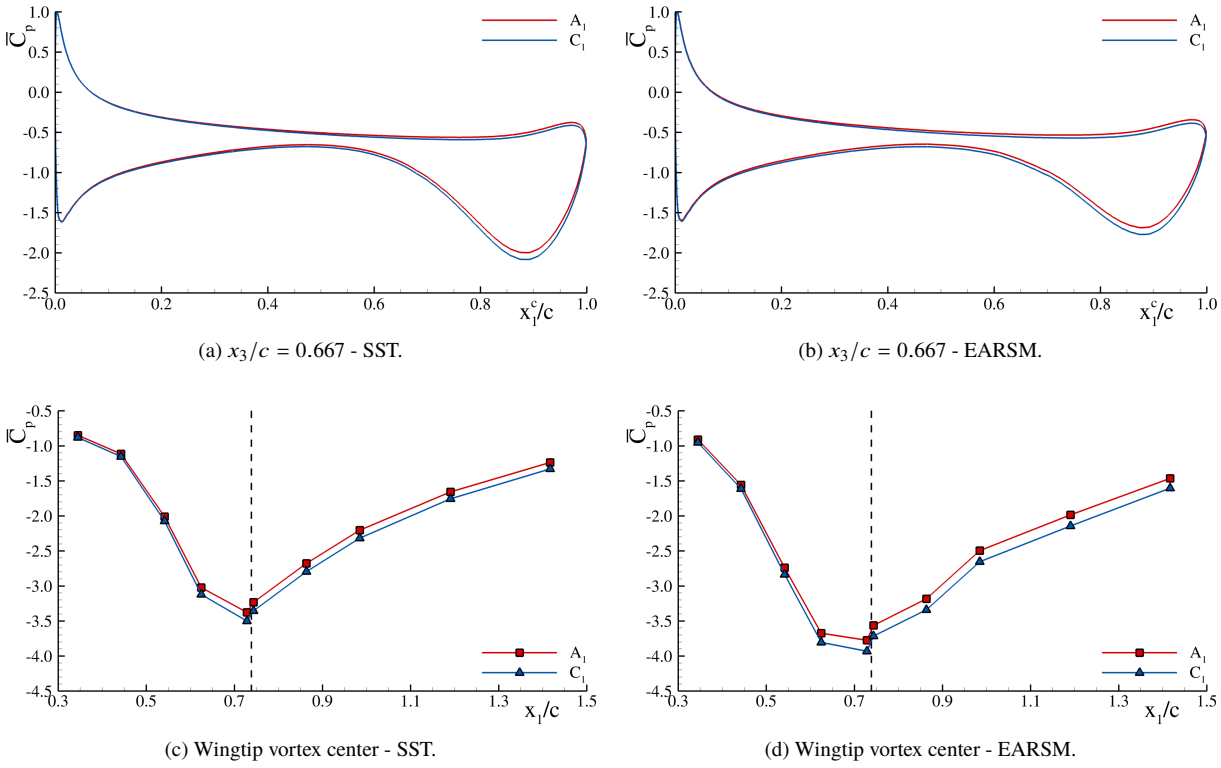

(a) x_3/c = 0.667 - SST.

(b) x_3/c = 0.667 - EARSM.

(c) Wingtip vortex center - SST.

(d) Wingtip vortex center - EARSM.

Fig. 7 Time-averaged pressure coefficient $\overline{C}_p$ along the wing's chord at cross-section x_3/c = 0.667, and at the experimentally determined wingtip vortex center as a function of the closure and numerical conditions: case A_1 - grid set A, and free-slip conditions at the wind tunnel's walls; and case C_1 - grid set C, and no-slip conditions at the wind tunnel's walls. Black dotted line indicates the x_1/c coordinate of the wing's trailing edge. Results in grid g_7.

reason, and considering the necessary grid resolution and the difficulties to define appropriate boundary-layers at the inlet plane, the remainder simulations neglect the effects of the boundary-layers at the test-section's walls.

B. Reynolds-Averaged Navier-Stokes Equations

The accuracy of the selected RANS closures in prediction of the wingtip flow is examined here. Towards this end, Section III.B.1 investigates the influence of the grid resolution for each model, whereas Section III.B.2 compares all closures with the experiments of Chow et al. [8]. The results shown in the latter section are obtained in the finest spatial resolution available - g_1 for RSM and g_3 for all turbulent viscosity closures.

1. Influence of the Grid Resolution

The large gradients involved in wingtip flows turn the numerical simulation of these phenomena demanding. The quality of the numerical predictions is therefore strongly dependent on the discretization strategy, grid topology and resolution. The latter aspect is particularly relevant in simulations performed with CFD solvers optimized for complex flow configurations since the geometrical flexibility of these codes tends to limit their discretization strategies to

Table 5 Time-averaged pressure drag $\overline{C}_D$, friction drag $\overline{C}_F$, and pressure lift $\overline{C}_L$ coefficients, respective numerical uncertainty $U_n(\Phi)$, and comparison error $E_c(\Phi)$ as a function of the closure. Uncertainties shown as percentage of predicted value, while comparison error in percentage of the experimental value [8].

Closure	$\overline{C}_D \times 10^1$	$U_n(\overline{C}_D)$	$\overline{C}_F \times 10^2$	$U_n(\overline{C}_F)$	$\overline{C}_L$	$U_n(\overline{C}_L)$	$E_c(\overline{C}_L)$
SA	0.54	0.8	0.77	0.5	0.56	0.5	9.9
SA-C	0.54	0.9	0.76	0.5	0.56	0.5	10.0
W98	0.54	1.2	0.72	3.3	0.56	0.3	10.7
SST	0.55	1.1	0.75	4.1	0.57	0.8	11.2
TNT	0.55	1.6	0.77	2.9	0.57	1.9	11.1
KSKL	0.55	0.4	0.76	1.5	0.57	0.6	11.0
EARSM	0.55	1.8	0.70	2.0	0.57	1.9	11.0
RSM	0.55	0.8	0.75	1.5	0.57	0.6	11.7
Exp.[§]	–	–	–	–	0.51	–	–

second-order accuracy.

The aforementioned factors enhance the relevance of assessing the magnitude of the discretization error. Table 5 shows the results and respective numerical uncertainty for the friction and pressure coefficients obtained with the different RANS closures. Note that the numerical error is dominated by the discretization error due to the use of double precision and an iterative convergence criterion of 10^{-5} (10^{-7} for the RSM). The data of table 5 indicate a reduced influence of the discretization error in the prediction of these quantities. The estimated numerical uncertainties do not exceed 1.9% for the pressure coefficients, and 4.1% for the friction drag coefficient. Although not shown, this trend is further confirmed by the observed variation (data range) of less than 3.3% in $\overline{C}_D$, 7.7% in $\overline{C}_F$, and 1.8% in $\overline{C}_L$ upon grid refinement.

The influence of the discretization error is expected to grow in the prediction of local quantities, particularly for those measured in the wingtip vortex region. Figure 8 depicts the time-averaged pressure coefficient along the wing's chord at the cross-section $x_3/c = 0.667$ and at the wingtip vortex center for the SST, EARSM, and RSM closures. These three models are representative cases of the closures exhibiting the lowest (SST) and largest (EARSM and RSM) grid requisites. Regarding the pressure coefficient on the wing's surface, the results demonstrate the strong dependence of the $\overline{C}_p(x_1^c)$ predictions on the grid resolution. It is also clear that the grid requirements of the EARSM and RSM to achieve a small influence of the discretization error are significantly larger than those of the SST closure. Whereas the grid resolution of g_7 is sufficient to achieve small discretization errors in SST predictions, the EARSM and RSM require g_5 to attain similar differences. These trends are also observed for the time-averaged pressure coefficient at the wingtip vortex center. Yet, it is possible to distinguish a different trend between the EARSM and RSM closures. Whereas the

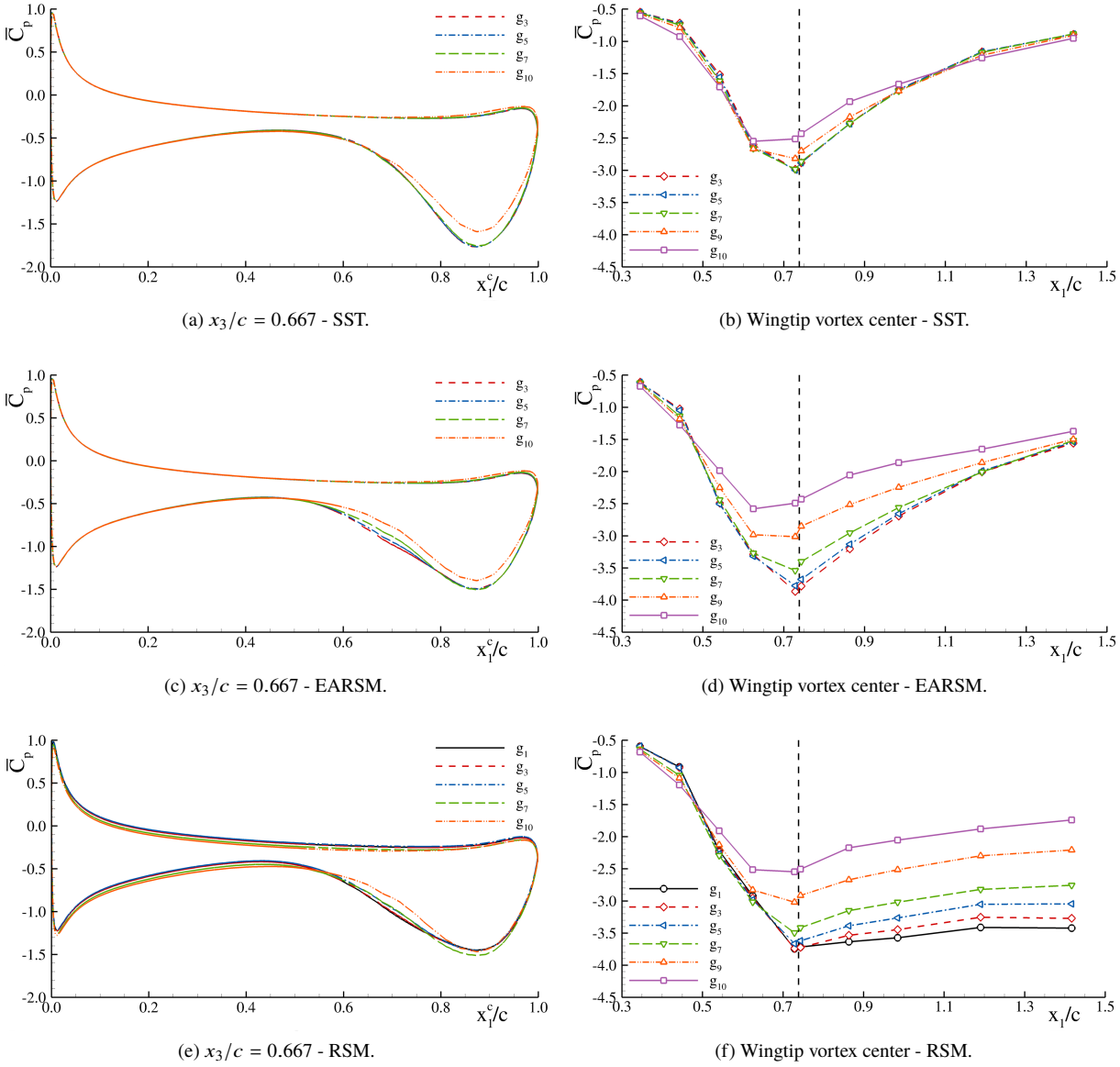

(a) $x_3/c = 0.667$ - SST.

(b) Wingtip vortex center - SST.

(c) $x_3/c = 0.667$ - EARSM.

(d) Wingtip vortex center - EARSM.

(e) $x_3/c = 0.667$ - RSM.

(f) Wingtip vortex center - RSM.

Fig. 8 Time-averaged pressure coefficient $\overline{C}_p$ along the wing's chord at the cross-section $x_3/c = 0.667$ and at the experimentally determined wingtip vortex center as a function of the spatial resolution. Black dotted line indicates the x_1/c coordinate of the wing's trailing edge. Results for the SST, EARSM and RSM closures.

EARSM and RSM closures exhibit similar variations upon grid refinement in the vicinity of the wing ($x_1/c \leq 0.74$), the grid requisites of RSM in the wingtip vortex wake region are substantially larger than for EARSM. Such result stems from the fact that the RSM predicts a stronger wingtip vortex which is inherently featured by steeper velocity gradients. For this reason, the grid requisites increase and solely the three finest grids possess sufficient resolution to make the RSM achieve reduced variations with the grid. This is the reasoning for using the two finest grids only with the RANS-RSM.

Overall, the prediction of local flow quantities in the wingtip vortex region is substantially more demanding than for integral quantities, requiring the use of the finest grids available to attain adequate magnitudes of the discretization error.

Table 6 Normalized multivariate metric r/r_{ref} for the time-averaged pressure coefficient $\overline{C}_p$ at the experimentally determined wingtip vortex center. Comparison error $E_c(\overline{C}_p)$ and numerical uncertainty $U_n(\overline{C}_p)$ are also presented for three streamwise locations: x_1/c = 0.442, 0.744, and 1.417. The superscript [1] indicates results obtained at the predicted wingtip vortex center (point of minimum $\overline{C}_p$). Uncertainties shown as percentage of predicted value, while comparison error in percentage of the experimental value [8].

Closure	x_1/c = 0.442		x_1/c = 0.744		x_1/c = 1.417		r/r_{ref}
	$E_c(\overline{C}_p)$	$U_n(\overline{C}_p)$	$E_c(\overline{C}_p)$	$U_n(\overline{C}_p)$	$E_c(\overline{C}_p)$	$U_n(\overline{C}_p)$	
SA	59.3	6.8	19.7	7.1	80.4	16.6	10.9
SA-C	57.1	8.8	3.6	9.3	42.3	41.4	5.3
W98	38.9	4.3	3.4	15.1	58.3	5.0	7.7
SST	53.1	16.0	16.6	2.0	75.4	27.5	10.6
TNT	54.0	28.5	13.9	2.8	66.6	7.1	12.8
KSKL	53.7	8.0	15.5	36.1	75.2	11.9	8.5
EARSM	32.9	19.5	-9.4	17.8	57.1	13.5	2.9
RSM	40.2	6.6	-7.5	8.8	5.8	44.8	2.6
RSM[1]	15.6	16.0	-10.1	6.5	2.4	33.1	1.0

Compared to the integral quantities of table 5, the resultant numerical uncertainties may increase one order of magnitude as demonstrated in table 6 for the time-averaged pressure coefficient at three points of the wingtip vortex center.

2. Modeling Accuracy

The modeling accuracy of the selected RANS closures to simulate the present wingtip flow is now discussed. To accomplish this objective, the predictions of integral and local flow quantities in the finest grid resolution are compared against the experiments of Chow et al. [8]. The resultant comparison error, uncertainties and multivariate metric r/r_{ref} are estimated for all quantities[‖], and the numerical uncertainty is calculated with the five finest grid resolutions available. The outcome of this study is presented in tables 5 and 6, and figures 9 to 12.

The friction and pressure coefficients, and respective numerical uncertainty, are shown in table 5. The predictions of the pressure coefficients exhibit a reduced influence from the closure strategy. The results vary less than 1.7% between all models. This trend, however, is not observed for the friction coefficient which varies up to 10.2% with the closure. Compared to the experiments, the lift coefficient is overpredicted by approximately 10% of the experimental measurement. Nonetheless, note that Chow et al. [8] estimated the lift coefficient from the pressure distribution along the wing's chord at only seven planes. It is then expected a significant experimental uncertainty in the estimated lift coefficient.

[‖] Those for $\overline{S}_{12}$ and $\overline{v_1 v_2}$ are not shown.

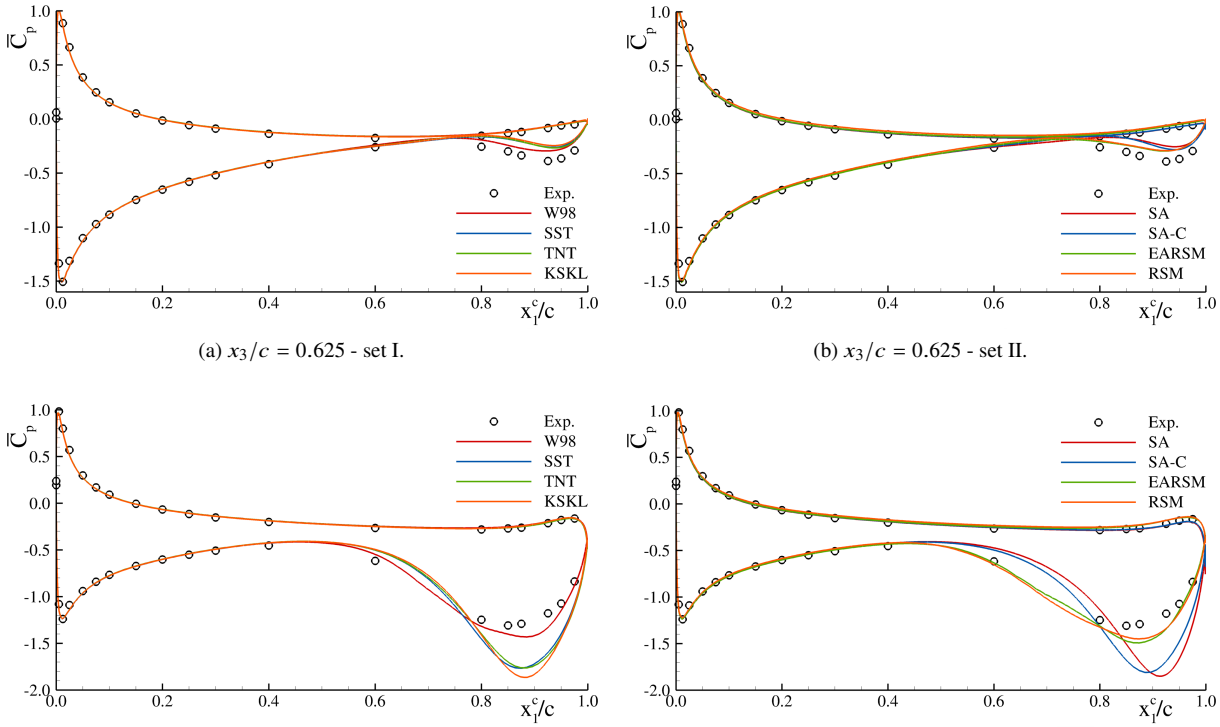

(a) $x_3/c = 0.625$ - set I.

(b) $x_3/c = 0.625$ - set II.

(c) $x_3/c = 0.667$ - set I.

(d) $x_3/c = 0.667$ - set II.

Fig. 9 Time-averaged pressure coefficient along the wing's chord $\overline{C}_p(x_1^c)$ as a function of the closure: set I - W98, SST, TNT, and KSKL; set II - SA, SA-C, EARSM, and RSM. Results at cross-section $x_3/c = 0.625$ and 0.667.

Figure 9 depicts the results of the pressure coefficient along the wing's chord at the cross-sections $x_3/c = 0.625$ and 0.667. The data show that all closures attain an excellent agreement with the experiments in the region not disturbed by the wingtip vortex - $x_1^c/c \leq 0.60$. Downstream $x_1^c/c = 0.60$, however, the wingtip vortex governs the flow dynamics. Consequently, most closures attain large comparison errors in this region owing to the inherent limitations of turbulent viscosity closures to predict near solid-body rotation. Solely the W98, EARSM, and RSM closures exhibit a good agreement with the experiments. The reasons for this outcome are addressed later.

The predictions of the pressure coefficient at the wingtip vortex center of figure 10 further illustrate the limitations of turbulent viscosity closures to predict such coherent structures. The selected modeling strategies lead to large comparison errors which may exceed in 80% the experimental measurement. In general, the formation of the vortex in the wing region is inaccurately represented, and its inner core is rapidly diffused downstream the trailing edge ($x_1/c \geq 0.74$). This behavior is particularly visible for the SA, SST and KSKL closures. The SA-C, W98, and EARSM, on the other hand, lead to a global enhancement of the predictions quality. It is also possible to distinguish two distinct trends in their results: *i)* only the EARSM and W98 closures seem able to improve the predictions in the wing region ($x_1/c \leq 0.74$); *ii)* although the three closures enhance the agreement with the experiments in the wake, the SA-C closure

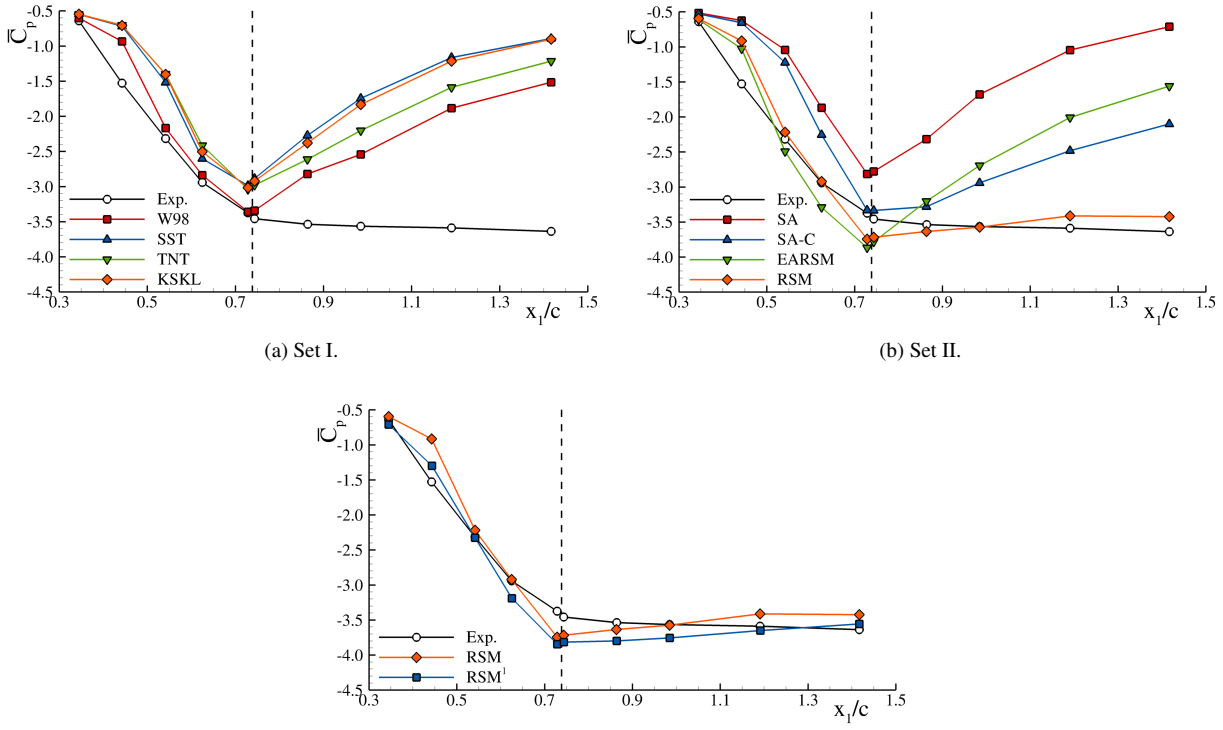

(a) Set I.

(b) Set II.

(c) RSM and RSM^1.

Fig. 10 Time-averaged pressure coefficient $\overline{C}_p$ at the experimentally determined wingtip vortex center as a function of the closure: set I - W98, SST, TNT, and KSKL; set II - SA, SA-C, EARSM and RSM. The superscript ^{1} indicates results obtained at the predicted wingtip vortex center (point of minimum $\overline{C}_p$) while the black dotted line the x_1/c coordinate of the trailing edge.

leads to the lowest comparison errors in this area. This stems from the fact that the correction employed in the SA-C model acts mostly in the wingtip wake region. The RSM closure, on the other hand, improves substantially the accuracy of the predictions, achieving a good agreement with the experimental measurements. The vortex is better represented in the wing's region ($x_1/c \leq 0.74$), and the pressure coefficient is almost constant in the wake which indicates that such structure is not being diffused as for the closures based on the Boussinesq hypothesis. Furthermore, it is important to mention that the location of the vortex center exhibits small mismatches between predictions (point of minimum $\overline{C}_p$) and experiments. Although these do not exceed $5.3c \times 10^{-3}$ and $2.6c \times 10^{-2}$ in the x_2 and x_3 directions, such small differences have a meaningful effect on the magnitude of the pressure coefficient as illustrated in figure 10c (or table 6).

The former conclusions are confirmed by table 6 which presents the outcome of the multivariate metric r/r_{ref} for the pressure coefficient at the wingtip vortex center. This strategy of quantifying the modeling error indicates that the SA-C, W98, and EARSM closures are able to improve the predictions of the pressure coefficient. Nonetheless, the magnitudes of r/r_{ref} also reaffirm that none of the selected turbulent viscosity closures is adequate to predict the wingtip vortex. Solely the second-moment closure RSM is able to achieve reduced values of r/r_{ref} which demonstrate its aptitude to accurately represent the mean-flow of this problem.

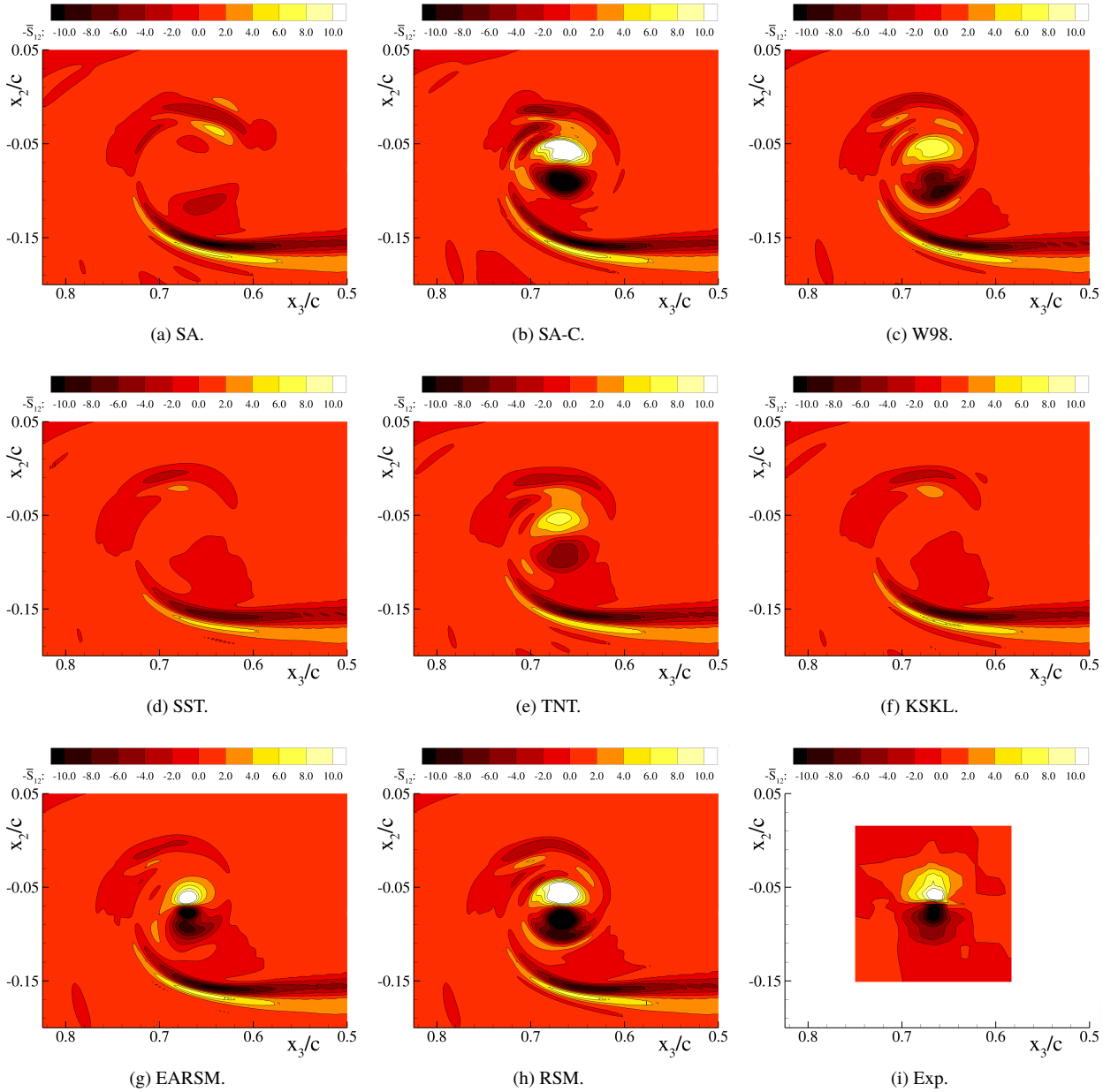

(a) SA. (b) SA-C. (c) W98.

(d) SST. (e) TNT. (f) KSKL.

(g) EARSM. (h) RSM. (i) Exp.

Fig. 11 Time-averaged strain-rate $\overline{S}_{12}$ shear component at $x_1/c = 0.985$ as a function of the closure. Experimental measurements taken from Chow et al. [8].

Finally, we consider the shear component of the time-averaged strain-rate $\overline{S}_{12}$ and Reynolds stress $\overline{v_1 v_2}$ tensors predicted by each closure at $x_3/c = 0.985$ - figures 11 and 12. The analysis of these two quantities points out the existence of six groups of models: *i)* SA, SST and KSKL - the predictions of $\overline{S}_{12}$ show that a significant part of the wingtip vortex has been already diffused at this location. This stems from the overprediction of the Reynolds-stress tensor which is particularly visible in figure 12a; *ii)* TNT - although the $\overline{v_1 v_2}$ are still excessive, the $\overline{S}_{12}$ field indicates that the wingtip vortex is less diffused. It is also clear that the quantities $\overline{v_1 v_2}$ and $\overline{S}_{12}$ are aligned; *iii)* W98 - the

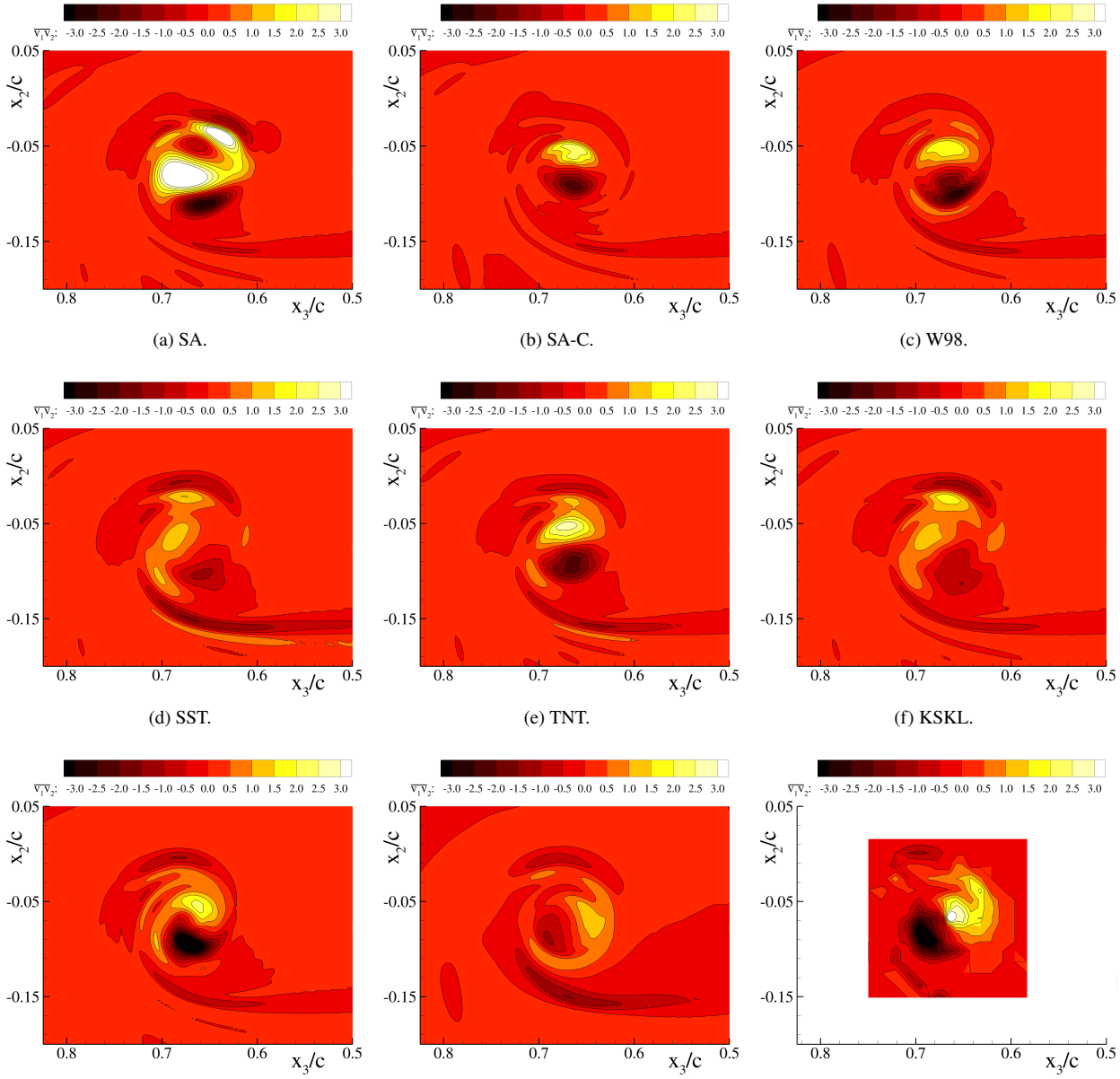

(a) SA. (b) SA-C. (c) W98.

(d) SST. (e) TNT. (f) KSKL.

(g) EARSM. (h) RSM. (i) Exp.

Fig. 12 Time-averaged Reynolds-stress $\overline{v_1v_2}$ shear component at $x_1/c = 0.985$ as a function of the closure. Experimental measurements taken from Chow et al. [8].

enhancement of its predictions is caused by the lower magnitudes of the Reynolds-stress tensor. However, this turbulent viscosity closure assumes the alignment of the strain-rate and Reynolds-stress tensor components; *iv)* SA-C - the observed improvement in the pressure coefficient in the wake region (figure 10) stems from an unphysical reduction of the magnitude of the Reynolds-stress tensor. Its components are clearly underpredicted. The maximum $\overline{S}_{12}$ predicted by this empirical approach is also slightly overpredicted; *v)* EARSM - although the comparison errors are still significant, the magnitude of Reynolds-stress $\overline{v_1v_2}$ is better predicted by this closure, showing some history effects, *i.e.* $\overline{v_1v_2}$ and

$\overline{S}_{12}$ are misaligned. Note that is not expected to an EARSM to fully capture history effects; *vi)* RSM - the strain-rate and Reynolds-stress tensor are no longer aligned and qualitatively agree with the experiments. Yet, $\overline{S}_{12}$ is slightly overpredicted while $\overline{v_1 v_2}$ is underpredicted. The latter result might be a consequence of discretization errors due to the use of a first order accurate discretization scheme in the governing equations of this closure. Therefore, the precise computation of $\overline{v_1 v_2}$ would require finer resolutions to guarantee negligible numerical errors.

Overall, none of the selected RANS approaches based on the Boussinesq hypothesis is able to accurately compute the wingtip vortex. Nonetheless, the EARSM and W98 demonstrate a fair agreement with the experiments in the wing's region. The curvature/rotation corrections described in Hellsten [50] and Smirnov and Menter [51] have also been tested in this investigation. These methods exhibited numerical robustness issues which precluded the reduction of the iterative error to the levels attained by the remainder closures. For this reason, the results of these approaches have not been shown. In regard to the RSM, the outcome of this study suggests such closure as the most adequate RANS approach to predict this wingtip vortex flow.

C. Scale-Resolving Simulations

The applicability of practical SRS methods to simulate the present wingtip flow is discussed here. Since the results of DXLES and PANS simulations exhibit similarities, DDES and DXLES/PANS computations are examined individually in Sections III.C.1 and III.C.2, respectively. All simulations are conducted in the spatio-temporal resolution g_5.

1. DDES Computations

Hybrid methods are pragmatic SRS strategies intended to simulate massively separated flows in an efficient manner. Towards this end, RANS is usually employed in boundary-layers, while outer and detached flow regions are simulated with a SRS method. The transition between these two regions generates an interface where the mathematical model alters from a fully statistical representation of turbulence, to an area where turbulence is partially resolved so that the Reynolds-stress tensor derives both from the resolved turbulent velocity field $\left(\overline{v_i v_j}\right)_r$ and the turbulence closure $\left(\overline{v_i v_j}\right)_u$,

$$\overline{v_i v_j} = \left(\overline{v_i v_j}\right)_r + \left(\overline{v_i v_j}\right)_u \ . \tag{2}$$

However, the sudden change in physical resolution causes a discontinuity in the Reynolds-stress tensor known as modeled stress depletion due to commutation errors. Its magnitude dictates the success of hybrid simulations, being strongly dependent on the mean-flow unsteadiness at the interface region. It is expected that a more unsteady mean-flow velocity field at the RANS/SRS interface diminishes the influence of the commutation error. In this manner, this issue constrains the use of hybrid formulations in flow problems not exhibiting massive separation. The present wingtip flow is certainly one of these cases due to the moderate angle of attack which does not lead to massive flow separation.

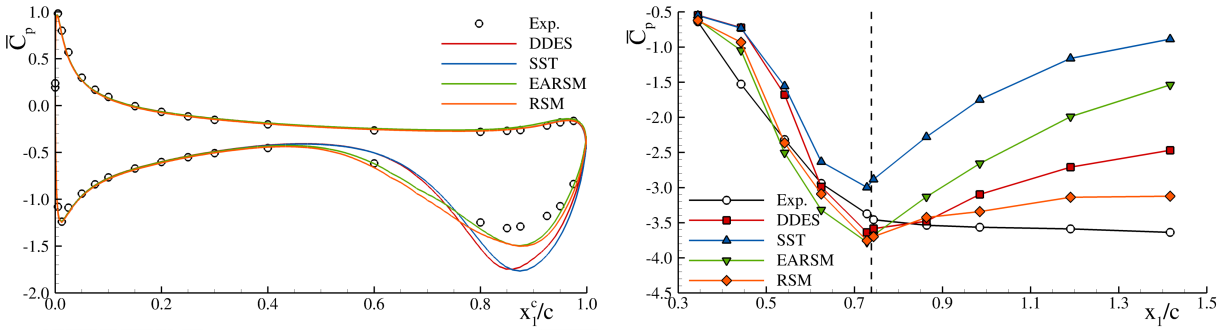

(a) $x_3/c = 0.667$.

(b) Wingtip vortex center.

Fig. 13 Time-averaged pressure coefficient $\overline{C}_p$ along the wing's chord at cross-section $x_3/c = 0.667$, and at the experimentally determined wingtip vortex centre for DDES and RANS methods in spatio-temporal resolution g_5. Black dotted line indicates the x_1/c coordinate of the trailing edge. Experimental measurements taken from Chow et al. [8].

Consequently, most turbulence is generated at the wing's surface, making the manner how turbulence is represented in the boundary-layers and the RANS/SRS interface determinant to the quality of the predictions.

The ability of hybrid models to predict the selected flow is now investigated through DDES computations. The results of the time-averaged pressure coefficient along the wing's chord at cross-section $x_3/c = 0.667$ and at the wingtip vortex center are shown in figure 13. The data indicate that the prediction of this quantity on the wing's surface is similar to that made by the RANS SST closure: an excellent agreement with the experiments until $x_1^c/c = 0.60$, whereas large comparison errors in the flow region disturbed by the wingtip vortex. This is an expected result since the boundary-layers are represented with RANS-SST. The wingtip vortex center, on the other hand, is better represented in the turbulent wake. DDES reduces the comparison error of RANS employing turbulent viscosity closures, and an eventual spatial resolution refinement is expected to further improve the results towards the experiments. Yet, the representation of the onset of this coherent structure is inaccurate for both RANS-SST and DDES. This is consequence of the wall proximity which limits the activation of the SRS mode. The comparison of DDES and RSM results in grid g_5 shows that the latter leads to a reduction of the comparison error which may exceed 50%.

The data of figure 13 suggest DDES as a possible alternative to traditional turbulent viscosity RANS closures. Nonetheless, the evaluation of the turbulent field and instantaneous quantities indicates that the observed improvement is simply a consequence of an unphysical reduction of the magnitude of the Reynolds-stress tensor. This point can be demonstrated in figure 14 where a component of the time-averaged strain-rate and Reynolds-stress tensors is plotted. Compared to the measurements of figures 11 and 12, the magnitude of $\overline{S}_{12}$ is similar to the experiments, while $\overline{v_1 v_2}$ is significantly underpredicted and aligned with $\overline{S}_{12}$. The reduced values of $\overline{v_1 v_2}$ stem from the fact that the portion of the Reynolds-stresses being resolved is of the order of the machine precision - $\left(\overline{v_i v_j}\right)_r \approx 0$. This issue derives from commutation errors at the RANS/SRS interface caused by the sudden transition between a statistically steady flow region

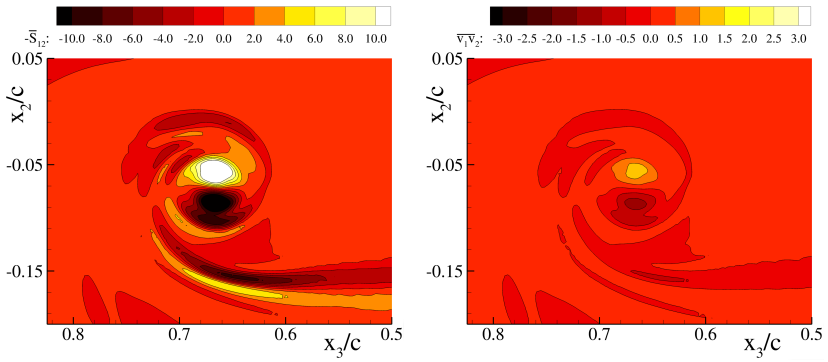

(a) $\overline{S}_{12}$. (b) $\overline{v_1 v_2} \times 10^3$.

Fig. 14 Time-averaged strain-rate $\overline{S}_{12}$ and Reynolds-stress $\overline{v_1 v_2}$ shear component at $x_1/c = 0.985$ for DDES in spatio-temporal resolution g_5.

(RANS) and an area where turbulence is partially resolved (SRS). In this manner, the absence of velocity fluctuations at the RANS/SRS interface leads to a Reynolds-stress tensor in the SRS zone composed solely of modeled turbulent stresses. It is possible that some of the techniques discussed, for instance, in Mocket et al. [52] could minimize this problem. Their assessment, however, is out of scope of this investigation.

Figure 15 depicts the resultant instantaneous velocity, shear-stress, and Q-criterion [53] fields. These fields exhibit the absence of significant unsteady features in most of the domain where the ratio between the smallest resolved and integral length scale l_t/l_t^{RANS} may reach 0.1. It is relevant to mention that the DDES calculation converged to this steady state after only ten time-units of simulation. Overall, although this type of computation may artificially reduce the comparison error, it is physically incorrect and cannot be used in a predictive manner.

2. DXLES and PANS Computations

This section concludes the discussion of the results with the outcome of the DXLES and PANS computations. It is important to stress that DXLES is a hybrid method relying on pure RANS and LES closures, whereas PANS is a bridging strategy where the same closure is used in the entire domain. Furthermore, note that the PANS simulations are conducted at constant physical resolution equal to $f_k = 0.50$ to avoid commutation errors, and DXLES usually leads to lower turbulent viscosity fields than the DDES model used in this study.

The two time-dependent simulations started from a partially converged DXLES solution, and run for ten time-units. The two boundary-layers are initially attached and the predicted flow quantities are converging towards the experiments of Chow et al. [8], *i.e.* the comparison error diminishes in comparison to turbulent viscosity RANS closures - see line $\Delta T V_\infty/c = 2.0$ in figure 16. After this initial period, the flow converges to a different state featured by a massive flow separation downstream the half chord of the wing - figure 17. The lift coefficient is reduced causing larger pressure coefficients at the wingtip vortex center as shown in figure 16. To understand the reasoning behind such outcome, recall

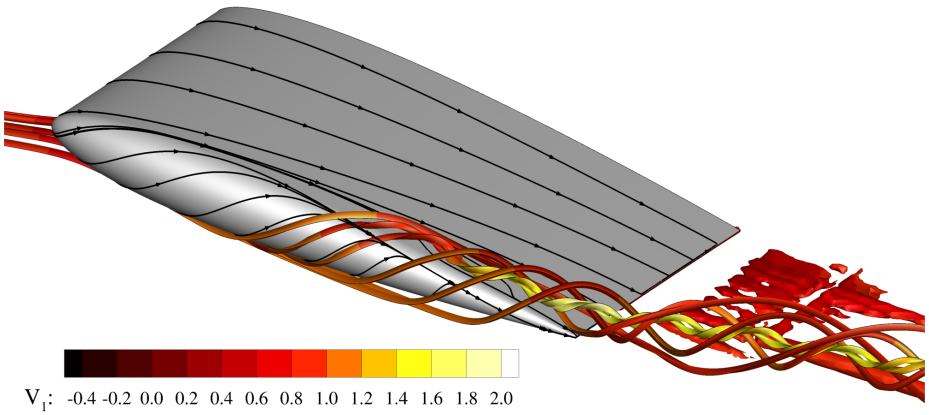

Fig. 15 Instantaneous wingtip vortex streamlines, limiting streamlines, and instantaneous Q-criterion iso-surfaces (Q = 1, 10, and 100) at the wing's wake for DDES. Results at $\Delta T V_\infty/c$ = 100 using spatio-temporal resolution g_5.

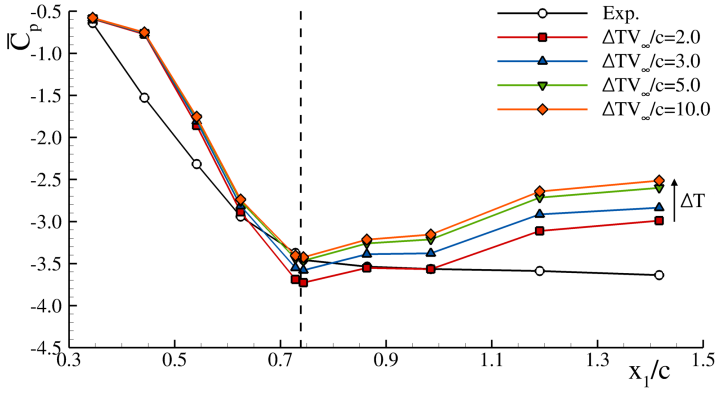

Fig. 16 Pressure coefficient $\overline{C_p}$ at the experimentally determined wingtip vortex center for DXLES and multiple time-instants, $\Delta T V_\infty/c$. Black dotted line indicates the x_1/c coordinate of the trailing edge. Results obtained in spatio-temporal resolution g_5.

that in Section II.A it was mentioned that the experiments of Chow et al. [8] used tripping elements to move turbulent transition from half chord to the vicinity of the leading edge - figure 2. Since transition is not forced in this investigation (nor in any of the studies of figure 1), formulations capable of resolving turbulence in boundary-layers move turbulence transition towards its natural location as the physical resolution increases. Along with the use of time-averaged inflow conditions, this aspect is the reason for the massive flow separation observed in PANS and DXLES simulations. The dimensions of the separation region are naturally dependent on the physical resolution. Consequently, the extension of the separation region increases with the physical resolution (determined by the magnitude of ν_t) - figures 17 and 18. Note that despite the hybrid nature of DXLES, this method leads to a significant reduction of ν_t in the boundary-layer region which is responsible for the aforementioned issues.

In summary, it has been shown that the predictive use of SRS methods to simulate the present wingtip steady flow is particularly challenging owing to the following aspects: *i)* the commutation errors generated at the RANS/SRS interface

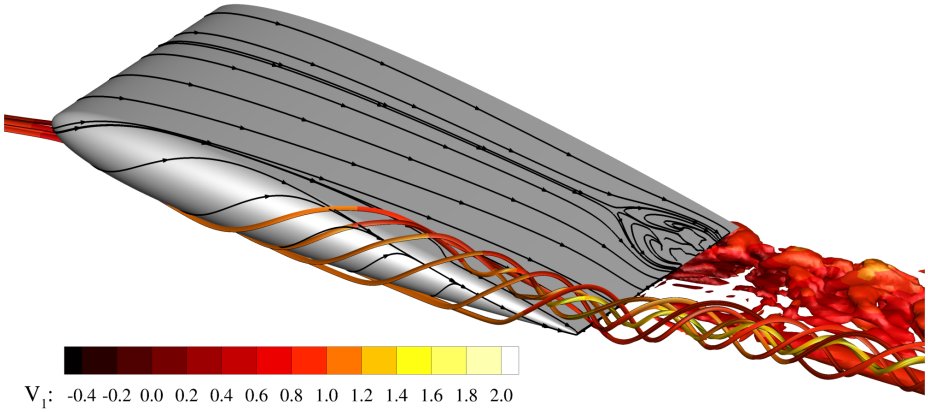

(a) DXLES.

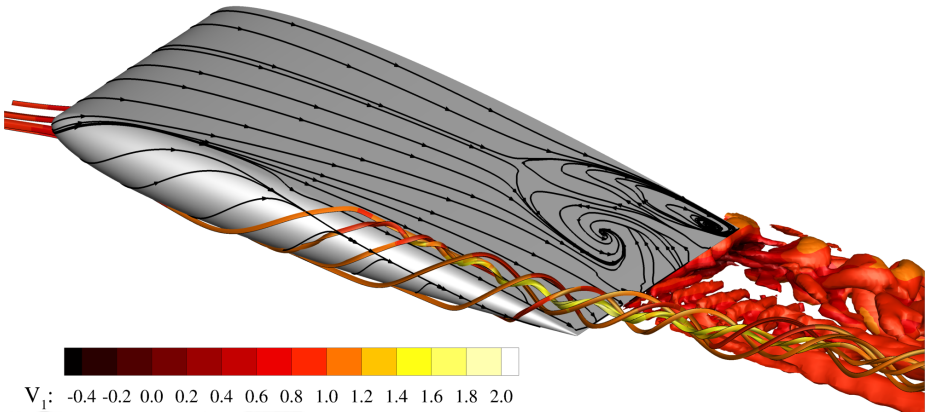

(b) PANS.

Fig. 17 Instantaneous wingtip vortex streamlines, limiting streamlines, and Q-criterion iso-surfaces (Q = 1, 10, and 100) at the wing's wake for DXLES and PANS (f_k = 0.50) methods. Results at $\Delta T V_\infty / c$ = 10 using spatio-temporal resolution g_5.

of hybrid formulations; and *ii)* forcing the onset of turbulence at the leading edge (and prescribe adequate unsteady inflow conditions) in bridging and hybrid formulations. The further investigation of these issues is not the objective of this study. For this reason, our SRS simulations used a single spatio-temporal resolution and a simulation time appropriate to address the aforementioned issues.

IV. Conclusions

This study has investigated the requisites and modeling accuracy of various RANS and SRS methods to simulate the flow around a rectangular wing with a NACA0012 section at $Re = 4.60 \times 10^6$ and ten degrees of angle of attack [8]. The selected modeling strategies range from turbulent viscosity and RSM RANS closures, to hybrid and bridging SRS approaches. The effect of replicating the experimental flow conditions is also examined. The major conclusions of this work are the following:

– independently of the turbulence closure, the location and conditions specified at the inlet boundary have a

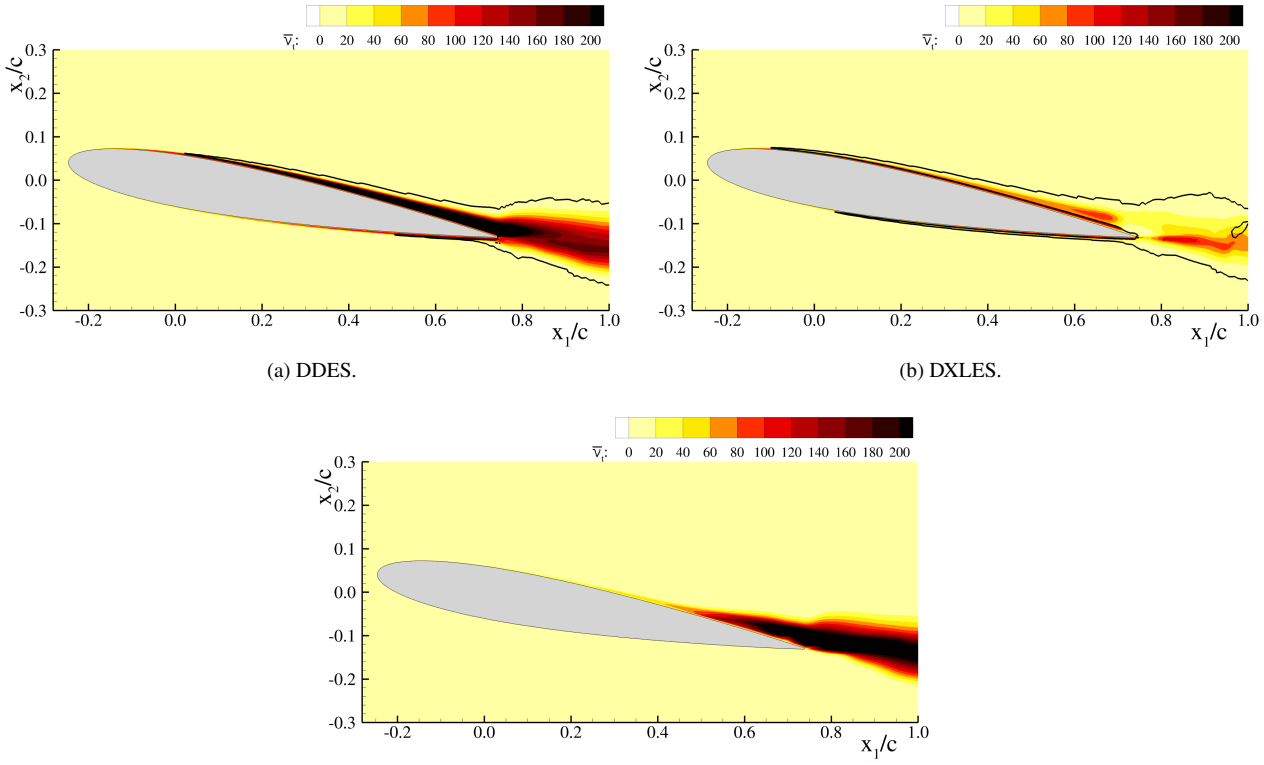

(a) DDES.

(b) DXLES.

(c) PANS.

Fig. 18 Instantaneous turbulent viscosity ν_t as a function of the selected SRS method at cross-section $x_3/c = 0.250$. SRS regions delimited by black line - $l_t/l_t^{\text{RANS}} = 0.999$. Results at $\Delta T V_\infty/c = 10$ using spatio-temporal resolution g_5.

significant impact on the simulations. It is observed that setting inflow conditions that do not match the velocity field at the inlet of the wind tunnel lead to undesirable inlet/modeling errors that cannot be attributed to the mathematical model. Therefore, the results show that from the several alternatives tested, the best approach is to replicate the experimental inflow conditions: match the location of the inlet of the wind tunnel and computational domain, and prescribe the measured velocity field. On the other hand, the effects of using free-slip instead of no-slip conditions at the side walls of the wind tunnel are weaker than those observed for the inlet conditions;

– the grid refinement level required to achieve adequate numerical uncertainties for local flow quantities in the wingtip vortex region is significantly larger than for functional drag and lift coefficients. The results ($N_c \leq 56.0 \times 10^6$) indicate that the numerical uncertainties for functional quantities do not exceed 4.1% whereas for local flow quantities these may grow one order of magnitude. Between all closures, the RSM exhibits the largest grid dependency owing to a significant increase in the vortex strength predicted by this closure which leads to larger velocity gradients;

– the selected RANS closures based on the Boussinesq hypothesis are not able to attain an overall good representation of this wingtip vortex flow. These lead to the largest comparison errors for the pressure in the wingtip vortex region,

and stem both from the alignment between the Reynolds-stress and strain-rate tensors and the overprediction of the turbulent stresses. For this reason, it is observed a trend where the smallest modeling errors are obtained for the closures leading to the lowest magnitudes of turbulent viscosity;

– the results indicate that solely RANS-RSM can achieve an accurate representation of the present flow problem. This closure leads to the smallest comparison errors of all modeling strategies tested, being the only formulation capable of replicating the behavior of the experimental pressure coefficient at the wingtip vortex core;

– in comparison to turbulent viscosity closures, the DDES model leads to a significant reduction of the comparison error in the prediction of local mean-flow quantities in the wingtip vortex region. However, this apparent improvement is simply a consequence of an unphysical reduction of the Reynolds-stress tensor due to commutation errors at the RANS/SRS interface. As a result, the flow in the SRS area converges to a statistically steady state where no turbulent fluctuations are observed so that the Reynolds-stress tensor is only composed of modeled turbulent stresses - $\left(\overline{v_i v_j}\right)_r \approx 0$;

– the tripping elements used in the experiments of Chow et al. [8] to move turbulence onset from the wing's half chord to the leading edge pose additional challenges to SRS methods resolving turbulence in boundary-layers. It is shown that not tripping the flow at the leading edge conducts to massive flow separation, and its magnitude increases with the physical resolution of the mathematical model. The effects of this issue are not relevant in RANS due to the traditional premature turbulent transition of its closures [32]. This indicates that a precise prediction of this flow problem with SRS methods requires forcing transition. This is ideally accomplished by including the experimental tripping elements in the problem setup or, alternatively, using numerical techniques (see for instance Schlatter and Örlü [54]).

Overall, the present study has illustrated the difficulties involved in the prediction of the present wingtip vortex flow. Whereas the examined turbulent viscosity RANS methods are inaccurate representing the flow dynamics of the wingtip vortex, the use of SRS methods is complex due to the numerical (spatio-temporal resolution, iterative convergence criterion, and simulation time) and modeling (inlet conditions and forcing turbulence onset) requisites involved in their adequate and predictive utilization. In this manner, RANS-RSM seems the most accurate and efficient strategy to evaluate the mean-flow of this statistically steady flow problem.

Acknowledgments

The authors would like to thank Gregory Zilliac and Peter Bradshaw for providing the experimental measurements used in this investigation, as well as to Gregory Blaisdell and Matthew Churchfield. The authors also acknowledge Jaap Windt and Maarten Kerkvliet for their help in grid generation, and the Maritime Research Institute Netherlands and the Laboratory for Advanced Computing at University of Coimbra for providing the necessary HPC resources.

References

[1] Spalart, P., "Airplane Trailing Vortices," *Annual Review of Fluid Mechanics*, Vol. 30, No. 1, 1998, pp. 107–138. doi: 10.1146/annurev.fluid.30.1.107.

[2] Arndt, R., "Cavitation in Vortical Flows," *Annual Review of Fluid Mechanics*, Vol. 34, No. 1, 2002, pp. 143–175. doi: 10.1146/annurev.fluid.34.082301.114957.

[3] Grow, T., "Effect of a Wing on Its Tip Vortex," *Journal of Aircraft*, Vol. 6, No. 1, 1969, pp. 37–41. doi:10.2514/3.43998.

[4] Mehta, R., and Cantwell, E., "Mean Flow and Turbulence Measurements in a Half-Delta Wing Vortex," *Fluid Dynamics Research*, Vol. 4, No. 2, 1988, pp. 123–137. doi:10.1016/0169-5983(88)90019-6.

[5] Chigier, N., and Corsiglia, V., "Wind-Tunnel Studies of Wing Wake Turbulence," *Journal of Aircraft*, Vol. 9, No. 12, 1972, pp. 820–825. doi:10.2514/3.59082.

[6] Stinebring, D., Farrel, K., and Billet, M., "The Structure of a Three-Dimensional Tip Vortex at High Reynolds Numbers," *Journal of Fluids Engineering*, Vol. 113, No. 3, 1991, pp. 496–503. doi:10.1115/1.2909524.

[7] Devenport, W., Rife, M., Liapis, S., and Follin, G., "The Structure and Development of a Wing-Tip Vortex," *Journal of Fluid Mechanics*, Vol. 312, 1996, pp. 67–106. doi:10.1017/S0022112096001929.

[8] Chow, J., Zilliac, G., and Bradshaw, P., "Turbulence Measurements in the Near Field of a Wingtip Vortex," Technical memorandum 110418, National Aeronautics and Space Administration (NASA), Ames Research Center, Moffet Field, United States of America, February 1997.

[9] Srinivasan, G., McCroskey, W., Baeder, J., and Edwards, T., "Numerical Simulation of Tip Vortices of Wings in Subsonic and Transonic Flows," *American Institute of Aeronautics and Astronautics (AIAA) Journal*, Vol. 26, No. 10, 1988, pp. 1153–1162. doi:10.2514/3.10022.

[10] de Jong, F., Govindan, T., Levy, R., and Shamroth, S., "Validation of a Forward Marching Procedure to Compute Tip Vortex Generation Process for Ship Propeller Blades," Technical report R88-920023-F, Scientific Research Associates, inc., Glastonbury, United States of America, August 1988.

[11] Dacles-Mariani, J., Zilliac, G., Chow, J., and Bradshaw, P., "Numerical/Experimental Study of a Wingtip Vortex in the Near Field," *American Institute of Aeronautics and Astronautics (AIAA) Journal*, Vol. 33, No. 9, 1995, pp. 1561–1568. doi:10.2514/3.12826.

[12] Dacles-Mariani, J., Kwak, D., and Zilliac, G., "On Numerical Errors and Turbulence Modeling in Tip Vortex Flow Prediction," *International Journal for Numerical Methods in Fluids*, Vol. 30, No. 1, 1999, pp. 65–82. doi:10.1002/(SICI)1097-0363(19990515)30:1<65::AID-FLD839>3.0.CO;2-Y.

[13] Bradshaw, P., "Effects of Streamline Curvature on Turbulent Flow," Technical report AGARD-AG-169, Advisory Group for Aerospace Research and Development (AGARD), London, United Kingdom, August 1973.

[14] Wilcox, D., and Chambers, T., "Streamline Curvature Effects on Turbulent Boundary Layers," *American Institute of Aeronautics and Astronautics (AIAA) Journal*, Vol. 15, No. 4, 1977, pp. 574–580. doi:10.2514/3.60662.

[15] Kim, S.-E., and Rhee, S., "Toward High-Fidelity Prediction of Tip-Vortex Around Lifting Surfaces - What Does it Take," *Proceedings of the 25th Symposium on Naval Hydrodynamics*, St John's, Canada, 2004.

[16] Craft, T., Gerasimov, A., Launder, B., and Robison, C., "A Computational Study of the Near-Field Generation and Decay of Wingtip Vortices," *International Journal of Heat and Fluid Flow*, Vol. 27, No. 4, 2006, pp. 684–695. doi: 10.1016/j.ijheatfluidflow.2006.02.024.

[17] Churchfield, M., and Blaisdell, G., "Reynolds Stress Relaxation Turbulence Modeling Applied to a Wingtip Vortex Flow," *American Institute of Aeronautics and Astronautics (AIAA) Journal*, Vol. 51, No. 11, 2013, pp. 2643–2655. doi:10.2514/1. J052265.

[18] Uzun, A., Hussaini, M., and Street, C., "Large-Eddy Simulation of a Wing Tip Vortex on Overset Grids," *American Institute of Aeronautics and Astronautics (AIAA) Journal*, Vol. 44, No. 6, 2006, pp. 1229–1242. doi:10.2514/1.17999.

[19] Lombard, J.-E., Moxey, D., Hoessler, J., Dhandapani, S., Taylor, M., and Sherwin, S., "Implicit Large-Eddy Simulation of a Wingtip Vortex," *American Institute of Aeronautics and Astronautics (AIAA) Journal*, Vol. 54, No. 2, 2016, pp. 506–518. doi:10.2514/1.J054181.

[20] Schauerhamer, D., and Robinson, S., "A Validation Study of OVERFLOW for Wing-Tip Vortices," *Proceedings of the 54th American Institute of Aeronautics and Astronautics (AIAA) Aerospace Sciences Meeting*, AIAA 2016-1782, San Diego, United States of America, 2016. doi:10.2514/6.2016-1782.

[21] Launder, B., "Second-Moment Closure and its Use in Modelling Turbulent Industrial Flows," *International Journal for Numerical Methods in Fluids*, Vol. 9, No. 8, 1989, pp. 963–985. doi:10.1002/fld.1650090806.

[22] Hanjalić, K., "Second-Moment Turbulence Closures for CFD: Needs and Prospects," *International Journal of Computational Fluid Dynamics*, Vol. 12, No. 1, 1999, pp. 67–97. doi:10.1080/10618569908940816.

[23] Leschziner, M., and Lien, F., *Closure Strategies for Turbulent and Transitional Flows*, B. Launder and N. Sandham ed., Cambridge University Press, Cambridge, United Kingdom, 2002, Chaps. 5 - Numerical Aspects of Applying Second-Moment Closure to Complex Flows, pp. 153–187. doi:10.1017/CBO9780511755385.

[24] Mor-Yossef, Y., "Robust Turbulent Flow Simulations Using a Reynolds-Stress-Transport Model on Unstructured Grids," *Computers & Fluids*, Vol. 129, 2016, pp. 111–133. doi:10.1016/j.compfluid.2016.02.010.

[25] Pereira, F., "Towards Predictive Scale-Resolving Simulations of Turbulent External Flows," Ph.D thesis, Instituto Superior Técnico, Lisbon, Portugal, March 2018.

[26] Breuer, M., "Effect of Inflow Turbulence on an Airfoil Flow with Laminar Separation Bubble: An LES Study," *Flow, Turbulence and Combustion*, 2018. doi:10.1007/s10494-017-9890-2.

[27] Churchfield, M., and Blaisdell, G., "Near Field Wingtip Vortex Computation Using the WIND Code," *Proceedings of the 44th American Institute of Aeronautics and Astronautics (AIAA) Aerospace Sciences Meeting and Exhibit*, AIAA 2006-633, Reno, United States of America, 2006. doi:10.2514/6.2006-633.

[28] Albrecht, P., Wu, D., Martin, A., Bunge, U., and Thiele, F., "IV Applications - Test Cases: 1 - NACA0012 Wing with Rounded Tip," *FLOMANIA - A European Initiative on Flow Physics Modelling. Results of the European-Union Funded Project, 2002-2004*, Notes on Numerical Fluid Mechanics and Multidisciplinary Design, Vol. 94, edited by W. Haase, B. Aupoix, U. Bunge, and D. Schwamborn, Springer-Verlag, Berlin, Germany, 2006, pp. 183–192.

[29] Churchfield, M., and Blaisdell, G., "A Reynolds Stress Relaxation Turbulence Model Applied to a Wingtip Vortex Flow," *Proceedings of the 49th American Institute of Aeronautics and Astronautics (AIAA) Aerospace Sciences Meeting*, AIAA 2011-663, Orlando, United States of America, 2011. doi:10.2514/6.2011-663.

[30] Windt, J., and Bosschers, J., "Influence of Local and Adaptive Mesh Refinement on the Tip Vortex Characteristics of a Wing and Propeller," *Proceedings of the VI International Conference on Computational Methods in Marine Engineering (MARINE2015)*, Rome, Italy, 2015, pp. 862–873.

[31] Pereira, F., Vaz, G., Eça, L., and Girimaji, S., "Simulation of the Flow Around a Circular Cylinder at $Re = 3900$ with Partially-Averaged Navier-Stokes Equations," *International Journal of Heat and Fluid Flow*, Vol. 69, 2018, pp. 234–246. doi:10.1016/j.ijheatfluidflow.2017.11.001.

[32] Wilcox, D., *Turbulence Modeling for CFD*, 3rd ed., DCW Industries, La Cañada, United States of America, 2006.

[33] ReFRESCO, 2018. URL `http://www.refresco.org/`.

[34] Spalart, P., and Allmaras, S., "A One-Equation Turbulence Model for Aerodynamic Flows," *Proceedings of the 30th American Institute of Aeronautics and Astronautics (AIAA) Aerospace Sciences Meeting and Exhibit*, AIAA-92-0439, Reno, United States of America, 1992. doi:10.2514/6.1992-439.

[35] Wilcox, D., *Turbulence Modeling for CFD*, 2nd ed., DCW Industries, La Cañada, United States of America, 1998.

[36] Menter, F., Kuntz, M., and Langtry, R., "Ten Years of Industrial Experience with the SST Turbulence Model," *Proceedings of the 4th Turbulence, Heat and Mass Transfer*, Antalya, Turkey, 2003, pp. 625–632.

[37] Kok, J., "Resolving the Dependence on Freestream Values for the $k - \omega$ Turbulence Model," *American Institute of Aeronautics and Astronautics (AIAA) Journal*, Vol. 38, No. 7, 2000, pp. 1292–1295. doi:10.2514/2.1101.

[38] Dol, H., Kok, J., and Oskam, B., "Turbulence Modelling for Leading-Edge Vortex Flows," *Proceedings of the 40th American Institute of Aeronautics and Astronautics (AIAA) Aerospace Sciences Meeting and Exhibit*, AIAA 2002-0843, Reno, United States of America, 2002. doi:10.2514/6.2002-843.

[39] Menter, F., Egorov, Y., and Rusch, D., "Steady and Unsteady Flow Modelling Using the $k - \sqrt{k}L$ Model," *Proceedings of the 5th Symposium on Turbulence, Heat and Mass Transfer (THMT5)*, Dubrovnik, Croatia, 2006, pp. 403–406. doi: 10.1615/ICHMT.2006.TurbulHeatMassTransf.800.

[40] Eisfeld, B., and Brodersen, O., "Advanced Turbulence Modelling and Stress Analysis for the DLR-F6 Configuration," *Proceedings of the 23rd American Institute of Aeronautics and Astronautics (AIAA) Applied Aerodynamics Conference*, AIAA 2005-4727, Toronto, Canada, 2005. doi:10.2514/6.2005-4727.

[41] Gritskevich, M., Garbaruk, A., Schütze, J., and Menter, F., "Development of DDES and IDDES Formulations for the $k-\omega$ Shear Stress Transport Model," *Flow, Turbulence and Combustion*, Vol. 88, No. 3, 2012, p. 431–449. doi:10.1007/s10494-011-9378-4.

[42] Kok, J., "A Stochastic Backscatter Model for Grey-Area Mitigation in Detached Eddy Simulations," *Flow, Turbulence and Combustion*, Vol. 99, No. 1, 2017, pp. 119–150. doi:10.1007/s10494-017-9809-y.

[43] Girimaji, S., "Partially-Averaged Navier-Stokes Model for Turbulence: A Reynolds-Averaged Navier-Stokes to Direct Numerical Simulation Bridging Method," *Journal of Applied Mechanics*, Vol. 73, No. 3, 2005, pp. 413–421. doi:10.1115/1.2151207.

[44] Pereira, F., Vaz, G., and Eça, L., "An Assessment of Scale-Resolving Simulation Models for the Flow Around a Circular Cylinder," *Proceedings of the 8th International Symposium on Turbulence, Heat and Mass Transfer (THMT15)*, Sarajevo, Bosnia and Herzegovina, 2015.

[45] Menter, F., "Two-Equation Eddy-Viscosity Turbulence Models for Engineering Applications," *American Institute of Aeronautics and Astronautics (AIAA) Journal*, Vol. 32, No. 8, 1994, pp. 1598–1605. doi:10.2514/3.12149.

[46] Menter, F., and Esch, T., "Elements of Industrial Heat Transfer Predictions," *Proceedings of the 16th Brazilian Congress of Mechanical Engineering (COBEM)*, Vol. 20, Uberlândia, Brazil, 2001, pp. 117–127.

[47] Eça, L., and Hoekstra, M., "A Procedure for the Estimation of the Numerical Uncertainty of CFD Calculations Based on Grid Refinement Studies," *Journal of Computational Physics*, Vol. 262, 2014, pp. 104 – 130. doi:10.1016/j.jcp.2014.01.006.

[48] Hills, R., "Model Validation: Model Parameter and Measurement Uncertainty," *Journal of Heat Transfer*, Vol. 128, No. 4, 2006, pp. 339–351. doi:10.1115/1.2164849.

[49] The American Society of Mechanical Engineers (ASME), *Multivariate Metrics - Supplement 1 of ASME V&V 20-2009*, The American Society of Mechanical Engineers, United States of America, 2016.

[50] Hellsten, A., "New Advanced $k-\omega$ Turbulence Model for High-Lift Aerodynamics," *American Institute of Aeronautics and Astronautics (AIAA) Journal*, Vol. 43, No. 9, 2005, pp. 1857–1869. doi:10.2514/1.13754.

[51] Smirnov, P., and Menter, F., "Sensitization of the SST Turbulence Model to Rotation and Curvature by Applying the Spalart-Shur Correction Term," *Journal of Turbomachinery*, Vol. 131, No. 4, 2009. doi:10.1115/1.3070573.

[52] Mocket, C., Haase, W., and Schwamborn, D. (eds.), *Go4Hybrid: Grey Area Mitigation for Hybrid RANS-LES Methods. Results of the 7th Framework Research Project Go4Hybrid, Funded by the European Union, 2013-2015*, Notes on Numerical Fluid Mechanics and Multidisciplinary Design, Vol. 134, Springer-Verlag, Berlin, Germany, 2018.

[53] Hunt, J., Wray, A., and Moin, P., "Eddies, Streams, and Convergence Zones in Turbulent Flows," *Proceedings of the 1988 Summer Program, Center for Turbulence Research, Stanford University*, Stanford, United States of America, 1988, pp. 193–208.

[54] Schlatter, P., and Örlü, R., "Turbulent Boundary Layers at Moderate Reynolds Numbers: Inflow Length and Tripping Effects," *Journal of Fluid Mechanics*, Vol. 710, 2012, pp. 5–34. doi:10.1017/jfm.2012.324.